







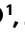





# Hypothalamic GABRA5-positive neurons control obesity via astrocytic GABA

Received: 23 December 2021

Accepted: 25 July 2023

Published online: 31 August 2023

 Check for updates

Moonsun Sa <sup>1,2</sup>, Eun-Seon Yoo <sup>3</sup>, Wuhyun Koh <sup>1</sup>, Mingu Gordon Park <sup>1</sup>, Hyun-Jun Jang <sup>4</sup>, Yong Ryoul Yang<sup>4</sup>, Mridula Bhalla <sup>1,5</sup>, Jae-Hun Lee<sup>1</sup>, Jiwoon Lim<sup>1,5</sup>, Woojin Won <sup>1</sup>, Jea Kwon<sup>1</sup>, Joon-Ho Kwon <sup>1</sup>, Yejin Seong <sup>1</sup>, Byungeun Kim<sup>6,7</sup>, Heeyoung An<sup>1</sup>, Seung Eun Lee<sup>8</sup>, Ki Duk Park<sup>6,7</sup>, Pann-Ghill Suh<sup>4</sup>, Jong-Woo Sohn <sup>3</sup> & C. Justin Lee <sup>1,2,5</sup> 

The lateral hypothalamic area (LHA) regulates food intake and energy balance. Although LHA neurons innervate adipose tissues, the identity of neurons that regulate fat is undefined. Here we show that GABRA5-positive neurons in LHA (GABRA5<sup>LHA</sup>) polysynaptically project to brown and white adipose tissues in the periphery. GABRA5<sup>LHA</sup> are a distinct subpopulation of GABAergic neurons and show decreased pacemaker firing in diet-induced obesity mouse models in males. Chemogenetic inhibition of GABRA5<sup>LHA</sup> suppresses fat thermogenesis and increases weight gain, whereas gene silencing of GABRA5 in LHA decreases weight gain. In the diet-induced obesity mouse model, GABRA5<sup>LHA</sup> are tonically inhibited by nearby reactive astrocytes releasing GABA, which is synthesized by monoamine oxidase B (Maob). Gene silencing of astrocytic Maob in LHA facilitates fat thermogenesis and reduces weight gain significantly without affecting food intake, which is recapitulated by administration of a Maob inhibitor, KDS2010. We propose that firing of GABRA5<sup>LHA</sup> suppresses fat accumulation and selective inhibition of astrocytic GABA is a molecular target for treating obesity.

Individuals with obesity have an imbalance in food intake and energy expenditure (EE), both of which are regulated by neural circuits that work inside the hypothalamus and extend beyond the hypothalamus<sup>1,2</sup>. The hypothalamus consists of a number of small nuclei, which include the lateral hypothalamic area (LHA). Although LHA occupies an extended field of the hypothalamus, it is substantially less anatomically defined<sup>3–6</sup>. A subpopulation of LHA neurons are known to innervate brown adipose tissue (BAT) and white adipose tissue (WAT) to mediate thermogenesis in BAT, browning of WAT and energy storage in WAT<sup>7,8</sup>. However, the precise cell types that innervate BAT and WAT to mediate thermogenesis and energy storage are still under active investigation.

The LHA contains several cell types expressing different transmitters and hormones, including neurons expressing melanin-concentrating hormone (MCH) and hypocretin/orexin<sup>9–11</sup>. MCH neurons in LHA negatively regulate BAT activity to suppress EE<sup>12</sup>, whereas orexin neurons send excitatory projections to increase BAT activity and EE with decreasing in food intake<sup>13–17</sup>. In addition, LHA contains other neurons that express neither MCH nor orexin<sup>18–20</sup>. A large population of GABAergic neurons in LHA are intrinsically depolarized and distinct from MCH and orexin<sup>19</sup>. These GABAergic neurons are defined by the presence of components necessary for GABA synthesis and release, including GAD65, GAD67 and vesicular GABA transporter<sup>21–25</sup>. Due to their location in LHA,

<sup>1</sup>Center for Cognition and Sociality, Institute for Basic Science, Daejeon, Republic of Korea. <sup>2</sup>KU-KIST Graduate School of Converging Science and Technology, Korea University, Seongbuk-gu, Seoul, Republic of Korea. <sup>3</sup>Department of Biological Sciences, Korea Advanced Institute of Science and Technology, Daejeon, Republic of Korea. <sup>4</sup>Ulsan National Institute of Science and Technology, Ulsan, Republic of Korea. <sup>5</sup>IBS School, University of Science and Technology, Daejeon, Republic of Korea. <sup>6</sup>Center for Brain Disorders, Brain Science Institute, Korea Institute of Science and Technology, Seoul, Republic of Korea. <sup>7</sup>Division of Bio-Medical Science and Technology, University of Science and Technology, Daejeon, Republic of Korea. <sup>8</sup>Virus Facility, Research Animal Resource Center, Korea Institute of Science and Technology, Seoul, Republic of Korea. ✉ e-mail: [cjl@ibs.re.kr](mailto:cjl@ibs.re.kr)

these neurons might participate in the regulation of energy balance. However, the classification and functional characterization of these GABAergic neurons in LHA remains to be explored<sup>26</sup>. Furthermore, how this heterogeneous population of GABAergic neurons in LHA interact with other cell types remains poorly understood.

It has been reported that the extracellular GABA level in the mediobasal hypothalamus is elevated during chronic over-nutrition<sup>27</sup>. However, how this extracellular GABA is synthesized and what causal role it plays in the pathogenesis of obesity and related metabolic syndrome remains to be elucidated. We have previously shown that monoamine oxidase B (Maob), mainly expressed in astrocytes, synthesizes astrocytic GABA<sup>28–30</sup>. Maob mediates degradation of polyamine putrescine, which is a byproduct of toxin degradation, to generate GABA in astrocytes<sup>30</sup>. Notably, a recent study found elevated levels of Maob in transcriptionally profiled LHA cells of high-fat diet (HFD)-fed mice<sup>31</sup>. Astrocytes are known to be actively involved in the regulatory aspects of metabolic control, such as feeding and brain glucose uptake<sup>32–39</sup>. In addition to their physiological role, increasing lines of evidence point to the involvement of hypothalamic astrocytes in the pathogenesis of diet-induced obesity (DIO)<sup>40</sup>. Reactive astrocytes are observed in several regions of hypothalamus after HFD feeding<sup>41</sup>. Consumption of dietary fats also induces metabolic damages in hypothalamic neurons, such as neuronal injury and a reduction of synaptic inputs to LHA<sup>2,42,43</sup>. However, the bridge between this neuronal dysfunction and reactive astrogliosis in LHA remains a mystery. Furthermore, the role of reactive astrocytes in LHA as the controller of pathological processes by over-nutrition still remains undetermined.

The response to released GABA from reactive astrocytes, conventionally called tonic GABA, is mediated by extrasynaptic GABA<sub>A</sub> receptors (GABA<sub>A</sub>Rs) in neighbouring neurons<sup>44</sup>. Tonic GABA reduces spike probability of granule cells in Alzheimer's disease (AD) mouse models<sup>45</sup>. Extrasynaptic GABA<sub>A</sub>Rs are composed of  $\alpha 5\beta 2$ ,  $\alpha 4\beta \delta$ ,  $\alpha 6\beta \delta$  and  $\alpha 1\beta \delta$  subunits and are located largely at extrasynaptic sites<sup>46,47</sup>. It has been previously demonstrated that  $\alpha 5$  subunit of GABA<sub>A</sub>R (GABRA5) shows moderate expression, whereas  $\delta$  subunit shows faint expression in LHA<sup>48</sup>. It has been further demonstrated that GABRA5-positive neurons are distinct from MCH, orexin A and orexin B in LHA<sup>20</sup>. However, whether these GABRA5-positive neurons in LHA (GABRA5<sup>LHA</sup>) are GABAergic and their physiological role in EE and food intake are entirely unknown.

In this Article, we hypothesized that GABRA5<sup>LHA</sup> play a regulatory role in energy balance by interacting with astrocytes via gliotransmitter GABA. On the basis of genetic, pharmacological and electrophysiological approaches, we found that GABRA5<sup>LHA</sup> are a distinct subpopulation of pacemaker-firing GABAergic neurons, regulating EE without affecting food intake via astrocytic GABA in HFD-fed mice. Given these findings, we suggest that genetic and pharmacological inhibition of excessive astrocytic GABA synthesis and GABA<sub>A</sub> receptor containing the  $\alpha 5$  subunit could be effective therapeutic strategies for obesity.

## Results

### Pacemaker firing in GABAergic GABRA5<sup>LHA</sup> is decreased in HFD

To identify and characterize the functional roles of GABRA5<sup>LHA</sup>, we developed GABRA5 promoter-containing virus and injected AAV-mGABRA5-EGFP-Cre into the LHA (Fig. 1a,b). Next, we performed immunohistochemical staining with antibodies against GABRA5, orexin A, orexin B, MCH and GABA in LHA-injected slices to confirm the specificity of the promoter. Most of GABRA5 promoter-containing enhanced green fluorescent protein (EGFP)-positive cells, indicating GABRA5-positive neurons, were overlapped with GABRA5 and GABA, but not with orexin or MCH (Fig. 1c,d). These results suggest that the GABRA5-promoter containing viruses specifically target GABRA5<sup>LHA</sup>, which are mostly GABA-producing neurons.

To investigate the intrinsic electrical properties of GABRA5<sup>LHA</sup>, we used whole-cell patch-clamp recordings in acute brain slices of

AAV-GABRA5-EGFP-Cre-injected mice (Fig. 1e–g). GABRA5<sup>LHA</sup> showed spontaneous activity and had a resting membrane potential near  $-50$  mV (Fig. 1h). We measured action potential (AP) wave forms from EGFP-positive neurons using sustained current injection (Fig. 1i). GABRA5<sup>LHA</sup> were spiking at near-threshold membrane potential and showed a maximum firing frequency of  $\sim 76$  Hz during maximal depolarization (Fig. 1j). It has been previously shown that LHA GAD65 cells fall into four subtypes on the basis of their distinct electrical signatures with evoked firing: fast spiking, late spiking (LS), low-threshold spiking (LTS) and regular spiking<sup>19</sup>. On the basis of this categorization, we characterized the firing patterns of GABRA5<sup>LHA</sup> before and after a hyperpolarizing current step (Fig. 1k). Approximately 66% of GABRA5<sup>LHA</sup> showed increased firing frequency after the step by more than 50% of that before the step. About 33% of GABRA5<sup>LHA</sup> did not start firing immediately after the step, but rather showed a slow ramp depolarization, resulting in a firing rate of less than 50% before the step (Fig. 1k,l). We found that GABRA5<sup>LHA</sup> fell into two major subtypes on the basis of their evoked firing (Fig. 1l). These results indicate that GABRA5<sup>LHA</sup> are LS and LTS subtypes of GAD65-positive GABAergic neurons in LHA.

To investigate the diet-induced changes in GABRA5<sup>LHA</sup>, we performed loose cell-attached patch clamping on GABRA5<sup>LHA</sup> without disturbing the intracellular ionic concentration in acutely prepared LHA slices from 8-week-old HFD-fed mice (Fig. 1m). We found that the GABRA5<sup>LHA</sup> pacemaker firing rate was significantly decreased in HFD mice (Fig. 1n,o). The decreased firing rate was substantially restored by treatment with the GABA<sub>A</sub> receptor antagonist, bicuculline (BIC, 50  $\mu$ M), in HFD mice (Fig. 1p,q). These results implicate GABA-mediated inhibition in tonically suppressing GABRA5<sup>LHA</sup> pacemaker firing in HFD mice.

### Inhibition of GABRA5<sup>LHA</sup> suppresses fat thermogenesis

We next investigated whether neuromodulation of GABRA5<sup>LHA</sup> regulates body weight and food intake by using chemogenetics to inhibit these neurons. We expressed the designer receptor exclusively inhibited by designer drug (DREADD) hM4Di specifically in GABRA5<sup>LHA</sup> by using a combination of AAV-mGABRA5-EGFP-cre and AAV-hSyn-DIO-hM4Di-mCherry viruses (Fig. 2a–c and Extended Data Fig. 1a,b). The DREADD system was confirmed using electrophysiology (Extended Data Fig. 1c,d) and immunohistochemistry (Extended Data Fig. 1e–h). After virus injection in LHA (Fig. 2a), the mice were fed HFD and administered clozapine *N*-oxide (CNO) by drinking for 5 weeks (Fig. 2b). Inhibition of GABRA5<sup>LHA</sup> by CNO led to a significant increase in body weight and food intake 4 weeks after virus injection (Fig. 2d–f). We then placed the mice in metabolic cages to enable automated phenotyping of whole-animal metabolic activity using the comprehensive laboratory animal monitoring system (CLAMS). Chemogenetic inhibition of GABRA5<sup>LHA</sup> led to no significant change in total EE (Fig. 2g–i), when using body weight as a covariant for analysis of covariance (ANCOVA) of EE<sup>49</sup>. There was also no significant change in locomotor activity (Fig. 2j,k). In addition, there was no significant difference in glucose tolerance (Fig. 2l,m), but partially impaired insulin sensitivity (Fig. 2n,o) in GABRA5::hM4Di compared with GABRA5::mCherry mice. We next examined the temperature of the BAT, located in the interscapular region, and the temperature of the tail (Fig. 2p). Remarkably, the BAT, but not the tail, temperature of GABRA5::hM4Di was significantly decreased compared with GABRA5::mCherry (Fig. 2q,r). Further, we examined the expression of candidate genes related to thermogenesis and lipolysis in adipose tissues by reverse transcription quantitative polymerase chain reaction (RT-qPCR) analysis using reference gene as 18 S ribosomal RNA<sup>15,50–54</sup>. Consistent with the metabolic changes, we found that GABRA5<sup>LHA</sup> inhibition led to a significant decrease in interscapular BAT (iBAT) messenger RNA levels of the uncoupling protein *Ucp1*, *Cidea* and *Dio2*, but not *Prdm16* or *Pgc-1 $\alpha$*  (Fig. 2s). There was also a significant decrease in the expression level of  $\beta$ -adrenergic receptor 3 (*Adrb3*) in inguinal WAT (iWAT) (Fig. 2t). These genes are important

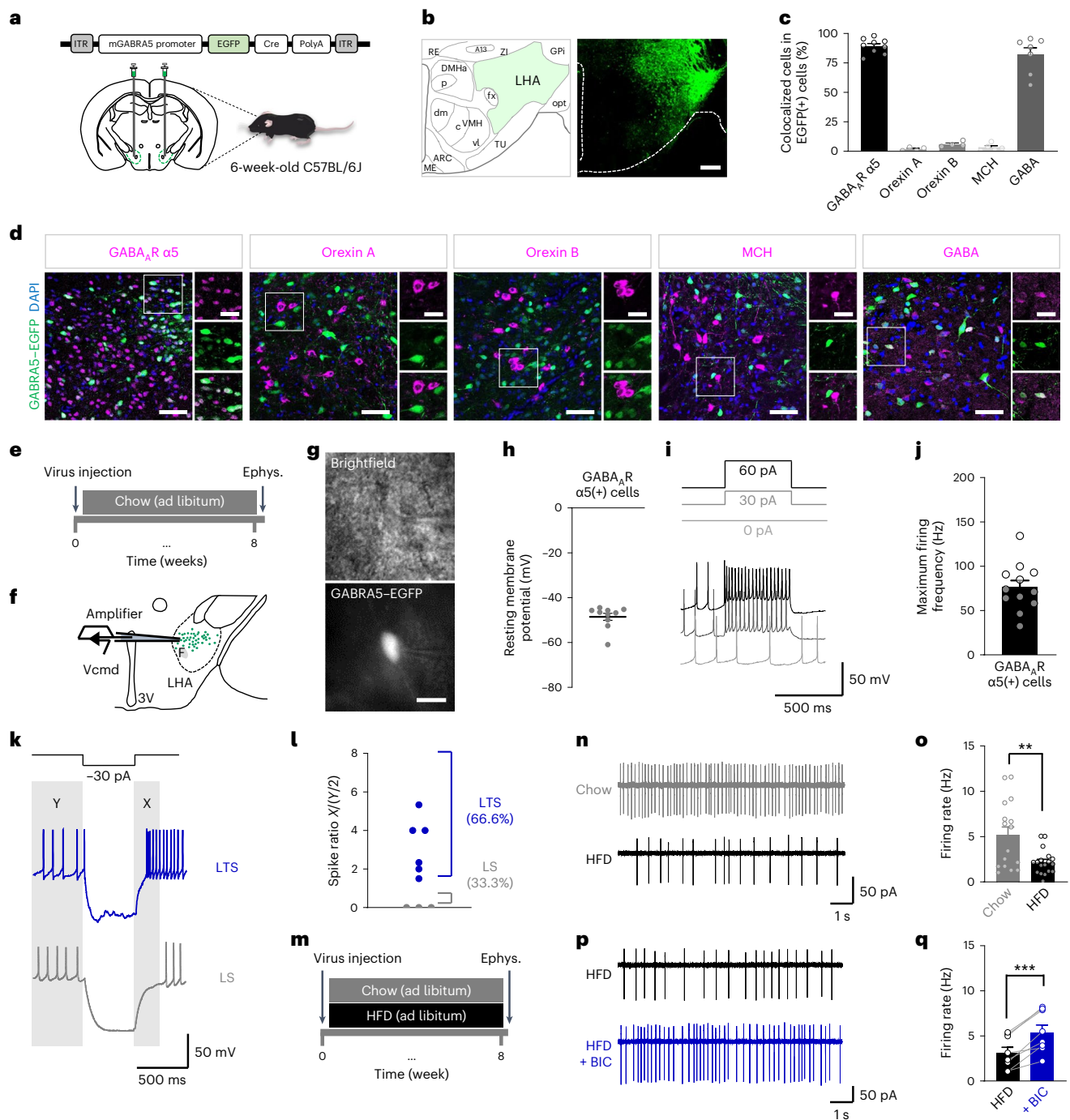


**Fig. 1 | GABAergic GABRA5<sup>LHA</sup> show decreased activity in HFD.** **a, b**, The experimental scheme (**a**) and representative image (**b**) for EGFP neurons infected with AAV-mGABRA5-EGFP-cre in LHA ( $n = 4$  mice). Bregma,  $-1.58$  mm AP. Scale bar,  $100 \mu\text{m}$ . ITR, inverted terminal repeats; RE, nucleus of reuiniens; ME, medial eminence; opt, optic tract; dm, dorsomedial part; c, central part; vl, ventrolateral part; p, posterior part; fx, columns of the fornix; A13, dopaminergic A13 group. **c**, Bar graph representation of quantification of colocalized cells in EGFP neurons. GABA<sub>A</sub>R  $\alpha 5$  ( $89.31 \pm 6.367$ ,  $n = 9$ ), orexin A ( $1.795 \pm 0.7482$ ,  $n = 4$ ), orexin B ( $5.9 \pm 1.135$ ,  $n = 4$ ), MCH ( $3.378 \pm 1.326$ ,  $n = 5$ ) and GABA ( $82.02 \pm 5.825$ ,  $n = 7$ ). **d**, Immunostaining images of LHA from AAV-mGABRA5-EGFP-cre (green) virus injected mice co-stained with GABRA5, orexin A, orexin B, MCH and GABA signals (magenta). Left, representative image with inset of region. Scale bar,  $100 \mu\text{m}$ . Right, magnified images from the boxes in the images on the left. Scale bar,  $50 \mu\text{m}$ . **e, f**, The timeline (**e**) and scheme of whole-cell patch clamp recording in GABRA5<sup>LHA</sup> (**f**). Ephys., electrophysiology; Vcmd, command voltage. **g**, Top, contrast and bottom, fluorescence micrograph of GABRA5<sup>LHA</sup> neuron being recorded. Scale bar,  $10 \mu\text{m}$ . **h**, Quantified resting membrane potentials (mV) of

GABRA5<sup>LHA</sup> based on  $I-V$ . GABA<sub>A</sub>R  $\alpha 5(+)$  cells ( $-48.52 \pm 1.571$ ,  $n = 10$  cells from 3 mice). **i**, Representative traces of non-fast spiking GABRA5<sup>LHA</sup> with depolarizing current steps. **j**, Maximal firing frequency of GABRA5<sup>LHA</sup> when a maximally depolarizing current step is applied. GABA<sub>A</sub>R  $\alpha 5(+)$  cells ( $76.14 \pm 7.738$ ,  $n = 12$  cells from 3 mice). **k**, Representative response of low-threshold spiking (LTS) (top) and late spiking (LS) (bottom) to the current step. Classification of non-fast spiking cells by hyperpolarizing current steps. **l**, Summary of spike ratio calculated from the X (250 ms) and Y (500 ms) time windows as spike amounts during X/(Y/2) ( $n = 9$  cells from 3 mice). **m**, Timeline for cell-attached patch-clamp recording in the GABRA5<sup>LHA</sup> experiment. **n**, Representative traces of cell-attached recording in GABRA5<sup>LHA</sup> from chow diet (top) and HFD (bottom) mouse. **o**, Quantification of firing rate between chow and HFD ( $n = 16$  cells from 3 mice,  $n = 18$  cells from 3 mice). **p**, Representative traces of cell-attached recording in GABRA5<sup>LHA</sup> from HFD (top) and HFD with BIC (bottom). **q**, Quantification of firing rate between HFD and BIC added ( $n = 8$  cells from 3 mice, respectively). Data are presented as mean  $\pm$  s.e.m.  $P$  values were determined by an unpaired  $t$ -test (**o**) or paired  $t$ -test (**q**). \* $P < 0.05$ , \*\* $P < 0.01$ , \*\*\* $P < 0.001$ .

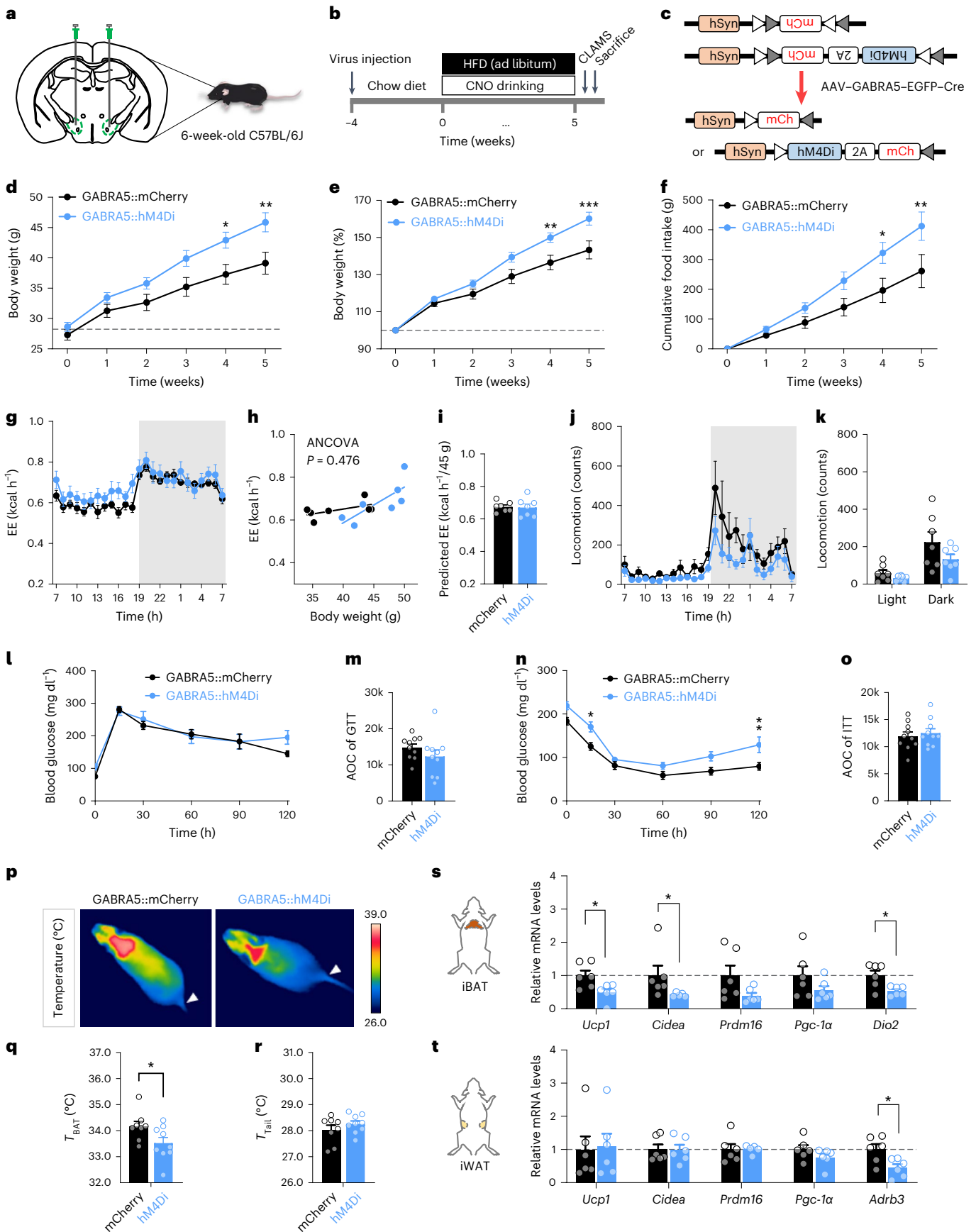


**Fig. 2 | Chemogenetic inhibition of GABRA5<sup>LHA</sup> suppresses fat thermogenesis.** **a, b**, Experimental scheme (**a**) and timeline (**b**) for GABRA5<sup>LHA</sup> under chemogenetic inhibition by DREADD hM4Di. **c**, Schematic diagram of GABRA5::mCherry (top) and GABRA5::hM4Di (bottom) virus construct before and after Cre recombination. **d**, Body weight on HFD with CNO drinking in grams ( $n = 7$  mice per group). GABRA5::mCherry versus GABRA5::hM4Di. **e**, Body weight on HFD with CNO drinking in percentage. **f**, Cumulative food consumption on HFD with CNO drinking. **g**, Real-time monitoring curve of EE in GABRA5::mCherry and GABRA5::hM4Di mice ( $n = 7$  mice per group). **h**, Regression of EE with body weight in GABRA5::mCherry and GABRA5::hM4Di mice. **i**, Predicted EE with 40 g body weight for each individual mouse, calculated by regression lines. **j**, Real-time monitoring curve of locomotion in GABRA5::mCherry and GABRA5::hM4Di mice with CNO drinking ( $n = 7$  mice per group). **k**, Quantification of locomotor activity in light and dark cycle. **l**, Time course of blood glucose levels during the GTT in GABRA5::mCherry and GABRA5::hM4Di mice ( $n = 10$  mice per group). The mean glucose concentrations during the GTT were compared at different

time points (0, 15, 30, 60, 90 and 120 min). **m**, Quantification of the AOC of GTT. **n**, Time course of blood glucose levels during the ITT in GABRA5::mCherry and GABRA5::hM4Di mice ( $n = 10$  mice per group). The mean glucose concentrations during the ITT were compared at different time points (0, 15, 30, 60, 90 and 120 min). **o**, Quantification of the AOC of ITT. **p**, Representative infra-red thermograph images showing the surface temperature of the intrascapular BAT ( $T_{BAT}$ ) and the tail temperature ( $T_{tail}$ ) in GABRA5::mCherry and GABRA5::hM4Di mice ( $n = 8$  and 9 mice, respectively). **q**, Quantification of  $T_{BAT}$ . **r**, Quantification of  $T_{BAT}$ . **s**, Molecular profiling of iBAT after chemogenetic inhibition of GABRA5<sup>LHA</sup> ( $n = 6$  samples per group). **t**, Molecular profiling of iWAT after chemogenetic inhibition of GABRA5<sup>LHA</sup> ( $n = 6$  samples per group). Data are presented as mean  $\pm$  s.e.m. *P* values were determined by two-way analysis of variance (ANOVA) with Sidák's multiple comparisons test (**d–g**, **j–l** and **n**), two-sided regression-based ANCOVA (**h**), two-tailed Mann–Whitney test (**i**, **s** and **t**) or unpaired *t*-test (**m**, **o**, **q** and **r**). \**P* < 0.05, \*\**P* < 0.01, \*\*\**P* < 0.001 and \*\*\*\**P* < 0.0001.

regulators of thermogenesis, browning and beiging of adipose tissue, and lipolysis<sup>52,53,55,56</sup>. To conclude, these results imply that chemogenetic inhibition of GABRA5<sup>LHA</sup> resulted in an increase in body weight with elevated food intake and decreased BAT thermogenesis, suggesting a potential redistribution of EE to tissues other than fat tissues while maintaining a consistent total EE.

### Gene silencing of GABRA5 in LHA reduces obesity

To assess whether GABRA5 regulates body weight and food intake, we employed gene silencing of *Gabra5* in LHA of HFD mice. We developed (Extended Data Fig. 2a–c) and injected lentivirus-carrying mouse *Gabra5*-specific short hairpin RNA (shRNA) into LHA (Fig. 3a–c), the knockdown efficiency of which was confirmed using immunohistochemistry (Extended Data Fig. 2d–f). Gene silencing of *Gabra5* (shGABRA5 group) gained significantly lesser body weight 5 weeks after injection (Fig. 3d), without affecting food intake, as compared with the control (Scrambled) group (Fig. 3f). To evaluate the changes in peripheral organs after gene silencing, we dissected key organs (Fig. 3e) and observed the weights of iWAT and perigonadal WAT (pWAT) were significantly lower in shGABRA5 mice (Fig. 3g). In contrast, the weights of liver, kidney, spleen, heart and quadriceps (quads) were not different in shGABRA5 mice compared with Scrambled mice (Fig. 3e, g). iBAT was slightly reduced in shGABRA5 mice, although it was not significantly different (Fig. 3h). Interestingly, the changes appeared only in HFD groups but not in chow diet groups (Extended Data Fig. 3a–l). To investigate the changes at the cellular level, we stained the adipose tissues with hematoxylin and eosin (H&E). The size of adipocytes in iWAT and pWAT was significantly smaller in shGABRA5 mice (Fig. 3i–l). iBAT histology also revealed significantly smaller lipid droplets of white adipocytes in shGABRA5 mice (Fig. 3m, n). To examine hepatic morphological alteration caused by gene silencing at the

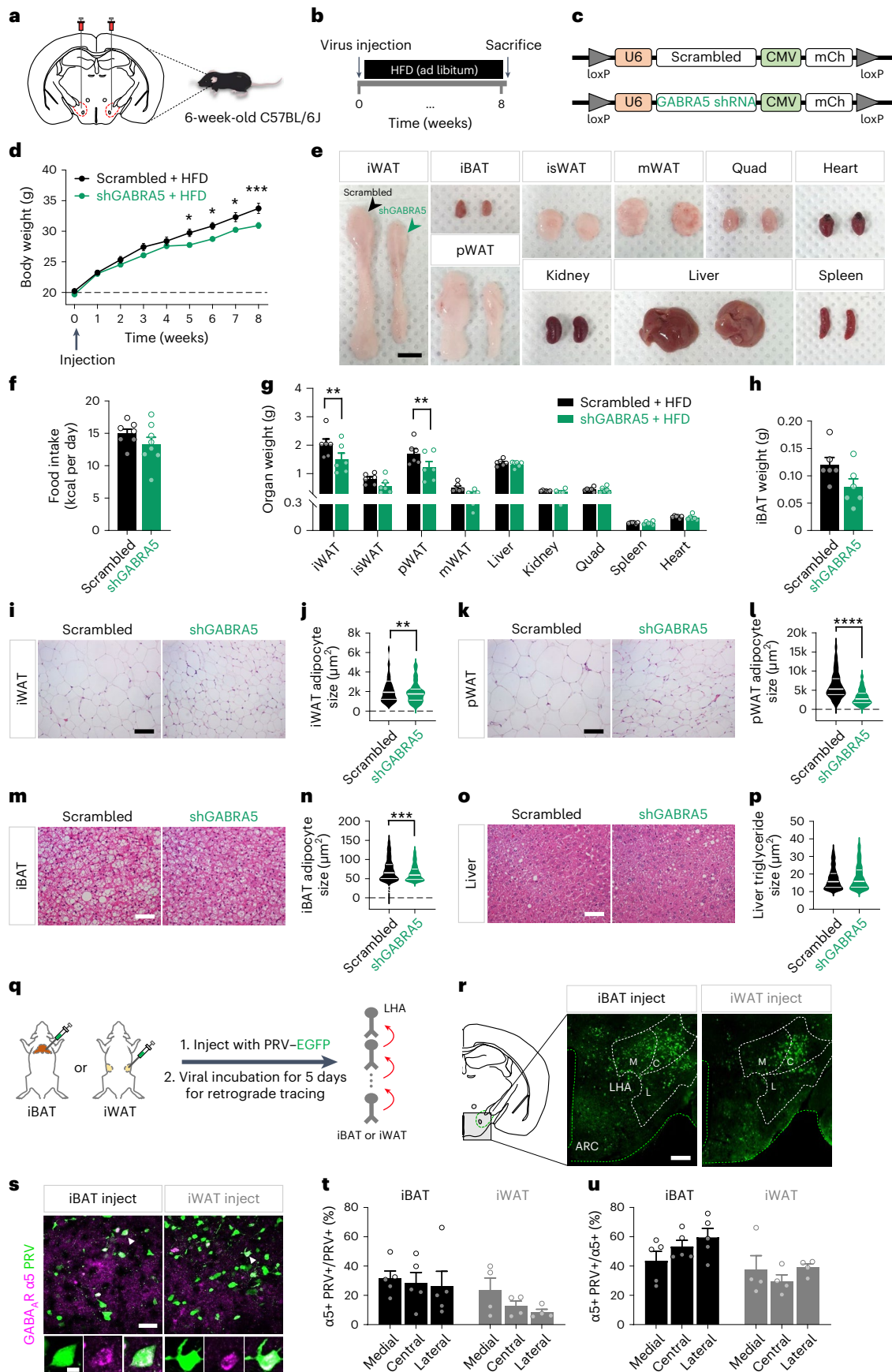
cellular level, we also observed hepatic cells using H&E staining. There was no significant change in lipid droplets in the hepatic cells (Fig. 3o, p). In addition, there was no significant difference in glucose tolerance and insulin sensitivity between shGABRA5 and Scrambled groups with HFD (Extended Data Fig. 3m–q), as well as with chow diet (Extended Data Fig. 3i–l). We observed that the shGABRA5 group had a significantly higher BAT temperature compared with the Scrambled group with HFD (Extended Data Fig. 3r–t). Taken together, these results indicate that gene silencing of *Gabra5* prevents the adipose tissue-specific weight increase due to HFD and chronic over-nutrition.

### GABRA5<sup>LHA</sup> polysynaptically project to BAT and WAT

To determine whether GABRA5<sup>LHA</sup> project to adipose tissues, we infected iBAT and iWAT with a recombinant pseudo rabies virus (PRV) that enables retrograde tracing of polysynaptically connected circuits<sup>57–59</sup>. The mice were killed 5 days after injection (Fig. 3q). In previous studies, several brain regions were found to project to iBAT and iWAT, including the primary sensory cortex, paraventricular hypothalamus, periaqueductal grey (PAG), LHA and raphe pallidus nucleus (RPa)<sup>57,59–61</sup>. Among these areas, we found that iBAT- or iWAT-projecting neurons were detected in the medial, central and lateral part of the caudal LHA (Fig. 3r and Extended Data Fig. 4a). Then, we performed immunohistochemistry to test whether iBAT- or iWAT-projecting neurons (EGFP positive) overlap with GABRA5-positive neurons within LHA. We observed that EGFP-positive cells were mainly distributed in the medial and central parts of LHA rather than the lateral part. Interestingly, we found that ~30% of the iBAT-projecting neurons and ~15% of the iWAT-projecting neurons overlapped with GABRA5 throughout LHA (Fig. 3s–u). These results indicate that there is a heterogeneity in the distribution of iBAT- and iWAT-projecting neurons within LHA. In addition, we observed that GABRA5<sup>LHA</sup> extend outside LHA (Extended

**Fig. 3 | Knockdown of *Gabra5* in LHA, innervating iBAT and iWAT, reduces obesity.** **a, b**, Experimental scheme (**a**) and timeline (**b**) for LHA injection. **c**, Schematic diagram of Scrambled (top) and shGABRA5 (bottom) virus constructs. CMV, cytomegalovirus promoter. **d**, Curves of body weight in Scrambled and shGABRA5 mice with HFD ( $n = 7$  and 8 per group, respectively). **e**, Representative images of each organ between Scrambled and shGABRA5 group. Scale bar, 1 cm. **f**, Average food intake per day in Scrambled and shGABRA5-injected mice. **g**, Quantification of organ weight in Scrambled and shGABRA5 groups ( $n = 6$  per group). **h**, Average weight of iBAT. **i, j**, H&E (**i**) of inguinal WAT and quantified adipose size (**j**) of iWAT of Scrambled and shGABRA5 group ( $n = 6$  mice per group). Scale bar, 100  $\mu$ m.  $n = 180$  and 262 cells, respectively. **k, l**, H&E (**k**) of perigonadal WAT, and quantified adipose size (**l**) of pWAT of Scrambled and shGABRA5 groups ( $n = 6$  mice per group). Scale bar, 100  $\mu$ m.  $n = 120$  and 180 cells, respectively. **m, n**, H&E (**m**) of interscapular BAT and quantified adipocyte size (**n**) of iBAT of Scrambled and shGABRA5 groups ( $n = 6$  mice per group). Scale bar,

100  $\mu$ m.  $n = 392$  and 391 cells, respectively. **o, p**, H&E (**o**) of liver and quantified triglyceride size (**p**) of liver of Scrambled and shGABRA5 groups ( $n = 6$  mice per group). Scale bar, 100  $\mu$ m.  $n = 732$  and 725 cells, respectively. **q**, Scheme for identifying LHA neurons that project polysynaptically to iBAT and iWAT. **r**, Confocal images for PRV-infected cells in LHA 5 days post-infection of PRV in iBAT and iWAT. Bregma,  $-1.58$  mm AP. Scale bar, 100  $\mu$ m. **s**, Immunostaining images of LHA from PRV-EGFP-injected (green) mice stained against GABA<sub>A</sub>R- $\alpha 5$  (magenta). Top, representative images of immunohistochemistry (IHC) in LHA regions. Scale bar, 50  $\mu$ m. Bottom, magnified images from the top, indicated by a white arrowhead. Scale bar, 10  $\mu$ m. **t, u**, Quantification between GABRA5 and PRV retrogradely labelled from iBAT and iWAT at 5 days post-injection ( $n = 5$  slices from 4 mice and 4 slices from 3 mice, respectively). Data are presented as mean  $\pm$  s.e.m. *P* values were determined by two-way ANOVA with Sidák's multiple comparisons test (**d** and **g**), unpaired *t*-tests (**f** and **h**) or Mann–Whitney test (**j**, **l**, **n** and **p**). \**P* < 0.05, \*\**P* < 0.01, \*\*\**P* < 0.001 and \*\*\*\**P* < 0.0001.



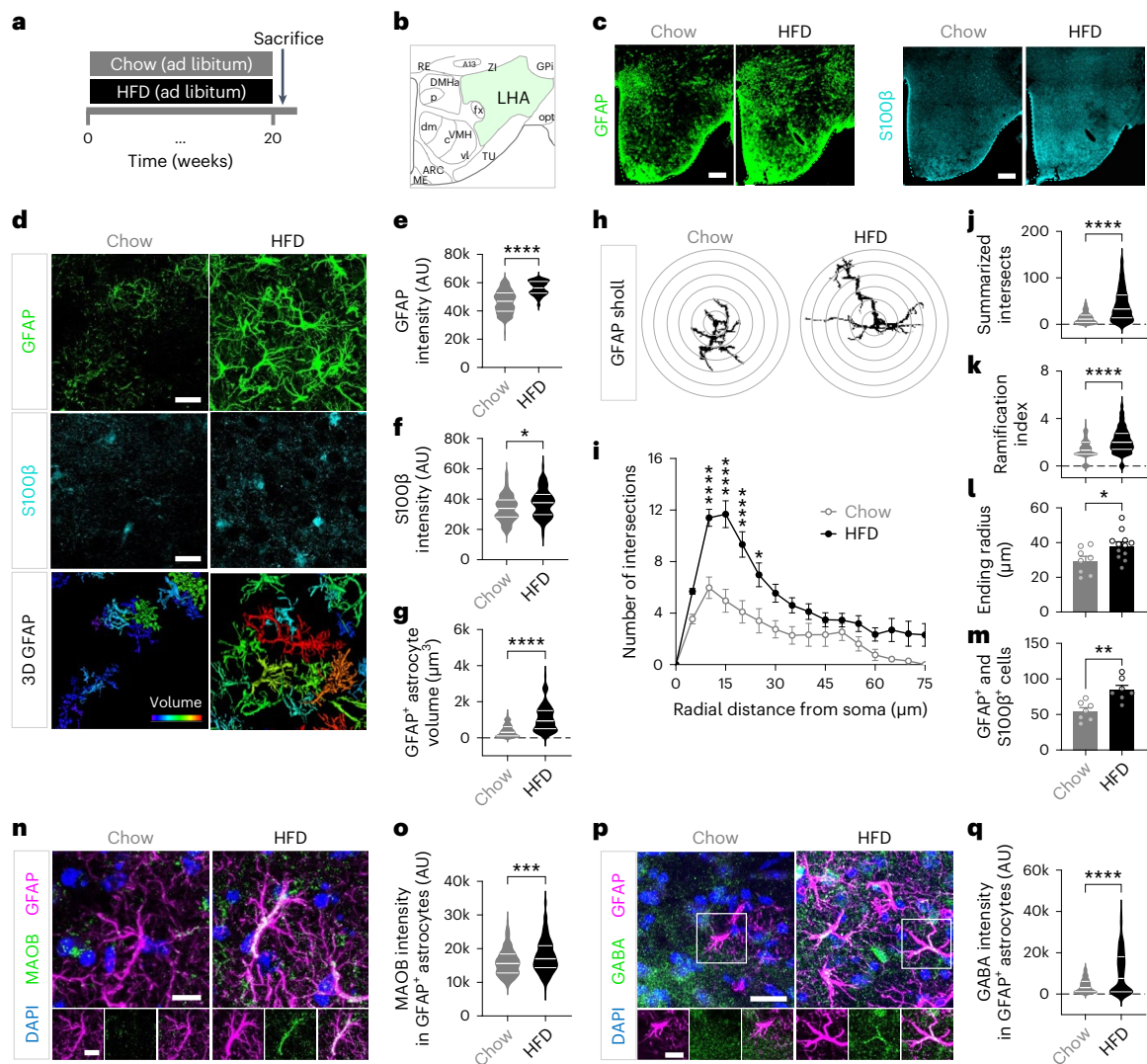


**Fig. 4 | Astrocytes in LHA show hypertrophy in response to HFD.** **a**, Timeline of two different diets; chow diet and HFD group. **b**, Brain atlas depicting LHA in the hypothalamus. **c**, Coronal images showing GFAP (green) and s100β (cyan) in chow and HFD mouse in LHA. Scale bar, 100 μm. **d**, Representative images of GFAP, s100β and 3D-GFAP in chow and HFD mice. Scale bar, 20 μm. **e**, A violin plot showing the quantification of GFAP intensity in chow and HFD mice ( $n = 152$  cells from 4 chow mice and  $n = 125$  cells from 6 HFD mice). **f**, A violin plot showing the quantification of s100β intensity ( $n = 78$  cells from 4 mice and 85 cells from 6 mice, respectively). **g**, Quantification of 3D volumes of GFAP<sup>+</sup> astrocytes in chow and HFD mice ( $n = 157$  cells from 4 mice and 99 cells from 6 mice, respectively). **h**, Representative images for Sholl analysis of an astrocyte in the LHA from the GFAP-stained image in **d**. The interval of the concentric circles is 1 μm. **i**, The number of process intersections at each radial distance from the soma in GFAP<sup>+</sup> astrocytes in the LHA of chow and HFD mice ( $n = 7$  slices from 4 mice and 12 slices from 6 mice, respectively). **j**, Number of summarized intersections of GFAP<sup>+</sup> astrocytes in chow and HFD mice ( $n = 381$  cells from 4 mice and 409 cells from

6 mice, respectively). **k**, The ramification index of GFAP<sup>+</sup> astrocytes in chow and HFD mice ( $n = 403$  cells from 4 mice and 411 cells from 6 mice, respectively). **l**, The ending radius of GFAP<sup>+</sup> astrocytes in LHA of chow and HFD mice ( $n = 8$  slices from 4 mice and 12 slices from 6 mice, respectively). **m**, The number of GFAP<sup>+</sup> and s100β<sup>+</sup> cells in the LHA of chow and HFD mice ( $n = 7$  slices from 4 mice and 7 slices from 6 mice, respectively). **n**, Immunostaining for Maob (green) and GFAP (magenta) in LHA of chow and HFD mice. Top: scale bar, 10 μm; bottom: scale bar, 10 μm. **o**, Quantification of Maob intensity in GFAP<sup>+</sup> astrocytes ( $n = 152$  cells from 4 mice and 152 cells from 6 mice). **p**, Immunostaining for GABA (green) and GFAP (magenta) in LHA of chow and HFD mice. Top: scale bar, 20 μm; bottom: images of GFAP, GABA and the merged overlay, taken from the boxes in the images on the top; scale bar, 10 μm. **q**, Quantification of GABA intensity in GFAP<sup>+</sup> astrocytes ( $n = 367$  cells from 4 mice and 338 cells from 6 mice). Data were presented as mean  $\pm$  s.e.m. *P* values were determined by Mann-Whitney tests (**e**, **g**, **j**, **k**, **m**, **o** and **q**), unpaired *t*-tests (**f** and **l**) or two-way ANOVA with Šidák's multiple comparisons (**i**). \**P* < 0.05, \*\**P* < 0.01, \*\*\**P* < 0.001 and \*\*\*\**P* < 0.0001.

Data Fig. 4b–d). This was further supported by the results from the tissue clearing and light-sheet microscopic images (Supplementary Video 1). Overall, these results imply that GABRA5<sup>LHA</sup> are involved in the innervation of iBAT and iWAT polysynaptically.

### Reactive astrocytes in LHA in response to HFD

Reactive astrocytes are observed in several regions of hypothalamus of HFD mice, such as arcuate nucleus (ARC), medial preoptic, paraventricular and dorsomedial hypothalamus (DMH)<sup>41</sup>. Unlike other

hypothalamic regions, reactive astrocytes in LHA are not defined yet. To determine the degree of astrogliosis in LHA, we made the mouse model with 20 weeks of HFD exposure. This duration of HFD exposure was chosen on the basis of the observation that almost all of the mice had undergone substantial weight gain, reaching saturated body weights exceeding 50 g. We examined the expression of astrocyte markers in LHA after 20 weeks of HFD feeding through immunohistochemistry (Fig. 4a). We found that astrocytes showed significantly hypertrophied signals in glial fibrillary acidic protein (GFAP) and S100β (Fig. 4b–f).

GFAP-positive astrocytes are abundantly observed at the edges of LHA, that is, in regions facing DMH, zona incerta (ZI) and internal globus pallidus (GPI) (Fig. 4c). This suggests that there is some degree of heterogeneity in reactive gliosis in LHA. The volume of GFAP-positive astrocytes significantly increased after three-dimensional (3D) rendering in HFD mice (Fig. 4d,g). Sholl analysis of individual astrocytes (Fig. 4h) showed that the summation of intersects (Fig. 4i,j), ramification index (Fig. 4k) and ending radius (Fig. 4l), which is an indicator of astrocytic territory, increased significantly in HFD compared with control mice. Additionally, the number of astrocytes, either GFAP-positive or S100 $\beta$ -positive cells in LHA (Fig. 4m), was significantly increased in HFD mice. Furthermore, we examined the astrogliosis after 8 weeks of HFD exposure. We specifically targeted a condition where the HFD group exhibited a moderate level of weight gain, approximately 40 g of body weight. The results showed a significant increase in astrogliosis in the HFD group after 8 weeks of HFD feeding (Extended Data Fig. 5a–j). Together, these results indicate that the astrocytes in LHA become reactive in response to a HFD, as evidenced by the prominent morphological hypertrophy.

We have previously reported that A $\beta$  plaques cause an increase in the activity of astrocytic Maob, which has been shown to produce GABA, leading to a decreased neuronal activity in animal models of AD<sup>45</sup>. On the basis of this previous report, we hypothesized that the reactive astrocytes in HFD mice would have high levels of Maob and GABA. We performed immunostaining in HFD mice and found that astrocytic Maob signals were significantly increased (Fig. 4n,o). We also observed that astrocytic GABA in HFD mice was significantly elevated (Fig. 4p,q and Extended Data Fig. 5e), with no change in neuronal GABRA5 level (Extended Data Fig. 5k–m). Taken together, these results indicate that Maob-mediated GABA in reactive astrocytes is significantly increased in LHA of HFD mice.

### Gene silencing of astrocytic Maob in LHA prevents obesity

We then hypothesized whether astrocyte-specific gene silencing of *Maob* in LHA can prevent DIO. To establish astrocyte-specific knockdown of *Maob*, we used Cre-dependent pSico–shMAOB with astrocyte-specific GFAP–cre viruses in LHA (shMAOB group) and Cre-dependent pSico–Scrambled virus as a control (Scrambled group) (Fig. 5a,c). The knockdown efficiency was previously confirmed by western blot in cultured astrocytes by ~60% (ref. 30) and confirmed by immunohistochemistry in LHA (Extended Data Fig. 5n,p). After providing both groups with HFD ad libitum for 8 weeks (Fig. 5b), we found shMAOB group gained significantly lesser body weight after 8 weeks of HFD feeding without affecting food intake (Fig. 5d,f). We next compared the weights of each organ between shMAOB and the Scrambled groups, and found that the shMAOB group exhibited significantly lower weight of iWAT, pWAT and BAT (Fig. 5e,g,h). Consistently, iWAT (Fig. 5i,j), pWAT (Fig. 5k,l) and BAT (Fig. 5m,n) histology revealed smaller lipid droplets

in the shMAOB group compared with the Scrambled group, with no significant change in the liver (Fig. 5o,p). This set of changes was not observed with chow diet (Extended Data Fig. 6a–h). Gene-silencing of *Maob* did not alter EE (Fig. 5q–s) or locomotor activity (Fig. 5t,u). In addition, there was no significant difference in glucose tolerance and insulin sensitivity between shMAOB and Scrambled groups with HFD (Extended Data Fig. 5q–t), as well as with chow diet (Extended Data Fig. 6i–l). Remarkably, the shMAOB group had a significantly higher temperature in the BAT, but not in the tail, compared with the Scrambled group (Fig. 5v–x), suggesting an increased heat production from the BAT. We also observed a significant increase in the expression of *Adrb3* in iWAT in shMAOB group (Fig. 5y,z). Furthermore, gene silencing of *Maob* did not alter the innervation of GABRA5<sup>LHA</sup> to iBAT (Extended Data Fig. 6m–p). Overall, gene silencing of LHA-specific astrocytic *Maob* enhances BAT thermogenesis and sympathetic tone in WAT, leading to the reduction in fat without compromising appetite or affecting EE in the HFD group.

### Gene silencing of astrocytic Maob in LHA reduces tonic GABA

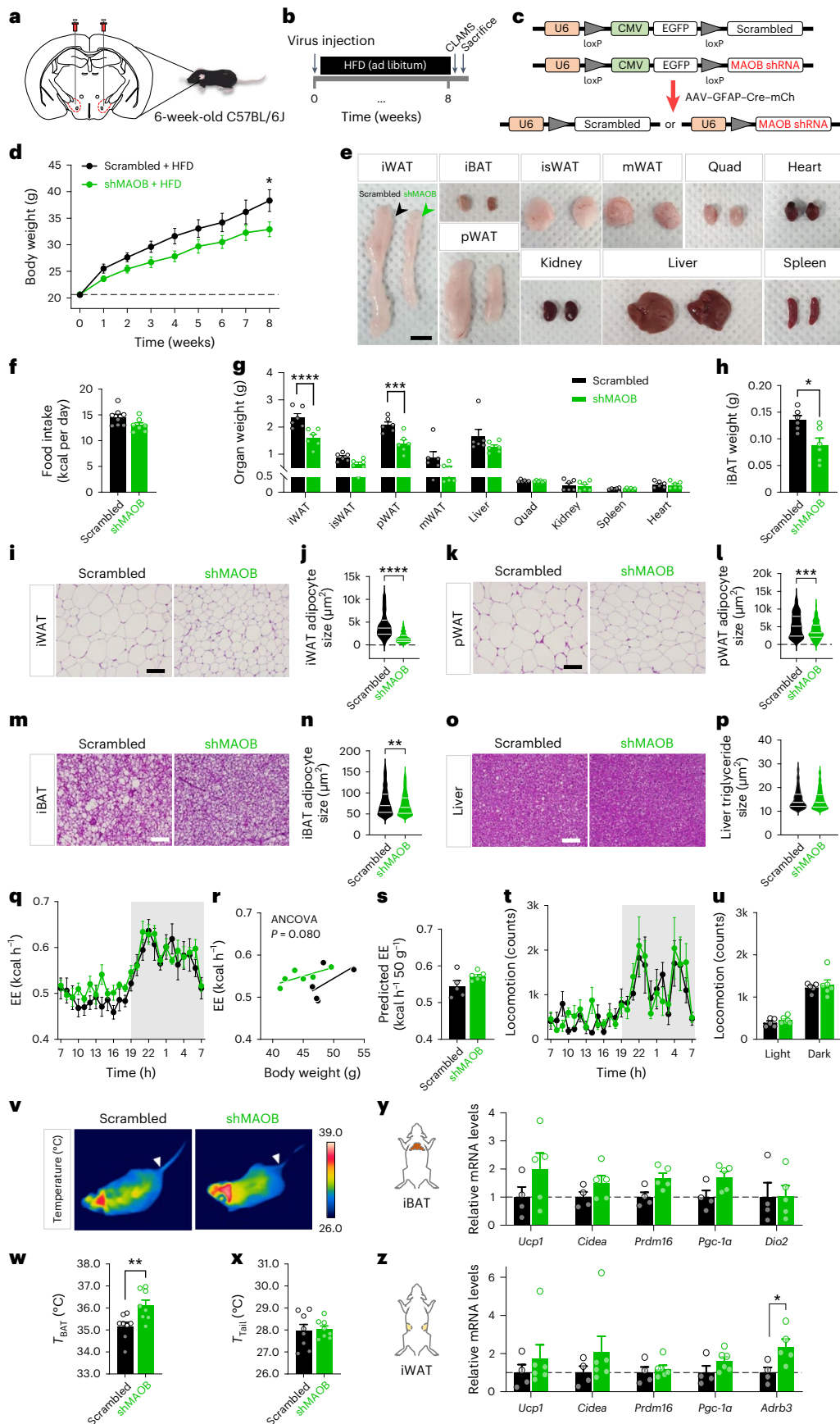
We observed that GABRA5<sup>LHA</sup> pacemaker firing is suppressed by GABA-mediated inhibition in HFD mice (Fig. 1n,o). The mode of GABA action can be either phasic or tonic inhibition<sup>62,63</sup>. Therefore, we investigated whether LHA cells were suppressed phasically (synaptically) or tonically (extrasynaptically). To test this possibility, we performed whole-cell patch-clamp recordings in the acutely prepared LHA slices (Fig. 6a). We assessed GABA<sub>A</sub> receptor-mediated phasic and tonic GABA currents by measuring the baseline current shift upon application of GABA<sub>A</sub>R antagonist, BIC (50  $\mu$ M), in the presence of ionotropic glutamate receptor antagonists, D-2-amino-5-phosphonovaleric acid (APV, 50  $\mu$ M) and 6-cyano-7-nitroquinoxaline-2,3-dione (CNQX, 20  $\mu$ M), as described previously<sup>45,64</sup>. The shMAOB group showed a significant decrease of tonic GABA current compared with the Scrambled group (Fig. 6b–d), suggesting gene silencing of *Maob* reduced tonic inhibition. There was decrease in the GABA-induced full-activation current, which was induced by 10  $\mu$ M GABA (Fig. 6e). The amplitude and frequency of spontaneous inhibitory post-synaptic currents (sIPSCs) were not significantly altered (Fig. 6f,g), indicating that phasic or synaptic GABA was not altered. The capacitance of LHA neurons was not affected by gene silencing of *Maob* (Fig. 6h). These results indicate that the action of GABA is mediated by tonic inhibition and astrocytic-specific gene silencing of *Maob* significantly attenuated the tonic inhibition. To investigate gene silencing of *Maob*-reduced astrocytic GABA, we performed immunohistochemistry in the shMAOB group. There was a significant reduction of astrocytic GABA in the LHA of the shMAOB group (Fig. 6i,m). We also performed a Sholl analysis of individual astrocytes to determine whether gene silencing of *Maob* reduces astrocytic reactivity. The Sholl analysis (Fig. 6j,k) showed that the summation of intersects (Fig. 6o) and ramification index

### Fig. 5 | Gene-silencing of astrocytic Maob in LHA prevents obesity.

**a,b**, Experimental scheme (**a**) and timeline (**b**) for LHA injection. **c**, Schematic diagram of Scrambled (top) and shMAOB (bottom) virus constructs before and after Cre recombination. **d**, Curves of body weight in Scrambled and shMAOB mice with HFD ( $n = 8$  and 7 mice, respectively). **e**, Representative images of each organ in Scrambled and shMAOB groups ( $n = 6$  per group). Scale bar, 1 cm. **f**, Average food intake per day in Scrambled and shMAOB mice. **g**, Quantification of organ weight for each organ in Scrambled and shMAOB groups ( $n = 6$  per group). **h**, Average weight of iBAT in Scrambled and shMAOB groups. **i,j**, H&E (**i**) of inguinal WAT and quantified adipose size (**j**) of iWAT of Scrambled and shMAOB groups ( $n = 6$  mice per group). Scale bar, 100  $\mu$ m.  $n = 138$  and 155 cells, respectively. **k,l**, H&E (**k**) of perigonadal WAT and quantified adipose size (**l**) of pWAT of Scrambled and shMAOB groups ( $n = 6$  mice per group). Scale bar, 100  $\mu$ m.  $n = 114$  and 147 cells, respectively. **m,n**, H&E (**m**) of iBAT and quantified adipose size (**n**) of iBAT of Scrambled and shMAOB groups ( $n = 6$  mice per group). Scale bar, 100  $\mu$ m.  $n = 580$  and 641 cells, respectively. **o,p**, H&E (**o**) of liver and quantified triglyceride size (**p**) of Scrambled and shMAOB groups ( $n = 6$  mice

per group). Scale bar, 100  $\mu$ m.  $n = 295$  and 569 cells, respectively. **q**, Real-time monitoring curve of EE in Scrambled and shMAOB mice ( $n = 5$  and 6 mice, respectively). **r**, Regression of EE with body weight in Scrambled and shMAOB mice. **s**, Predicted EE with 50 g body weight for each individual mouse, calculated by regression lines. **t**, Real-time monitoring curve of locomotion in Scrambled and shMAOB mice ( $n = 5$  and 6 mice, respectively). **u**, Quantification of locomotor activity in light and dark cycles. **v**, Representative infra-red thermograph images showing the surface temperature of the intrascapular BAT ( $T_{BAT}$ ) and the tail temperature ( $T_{tail}$ ) in Scrambled and shMAOB mice ( $n = 8$  mice per group). **w**, Quantification of  $T_{BAT}$ . **x**, Quantification of  $T_{tail}$ . **y**, Molecular profiling of iBAT in Scrambled and shMAOB mice ( $n = 4$  and 5 samples, respectively). **z**, Molecular profiling of iWAT in Scrambled and shMAOB mice ( $n = 4$  and 6 samples, respectively). Data are presented as mean  $\pm$  s.e.m.  $P$  values were determined by two-way ANOVA with Sidak's multiple comparisons (**d**, **g** and **u**), unpaired  $t$ -tests (**h**, **w** and **x**), Mann–Whitney tests (**f**, **j**, **l**, **n**, **p**, **s**, **y** and **z**) or two-sided regression-based ANCOVA (**r**). \* $P < 0.05$ , \*\* $P < 0.01$ , \*\*\* $P < 0.001$  and \*\*\*\* $P < 0.0001$ .





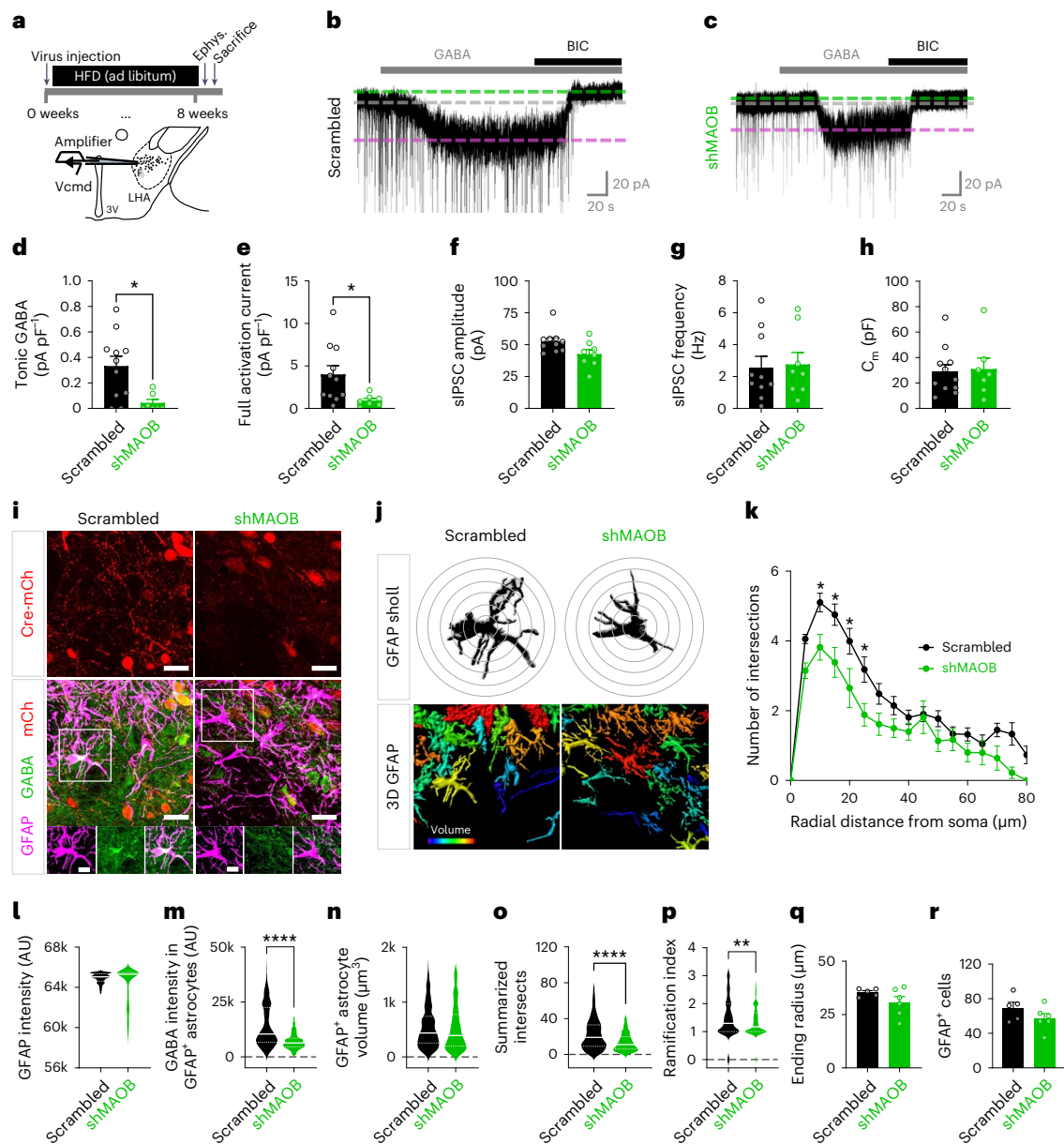


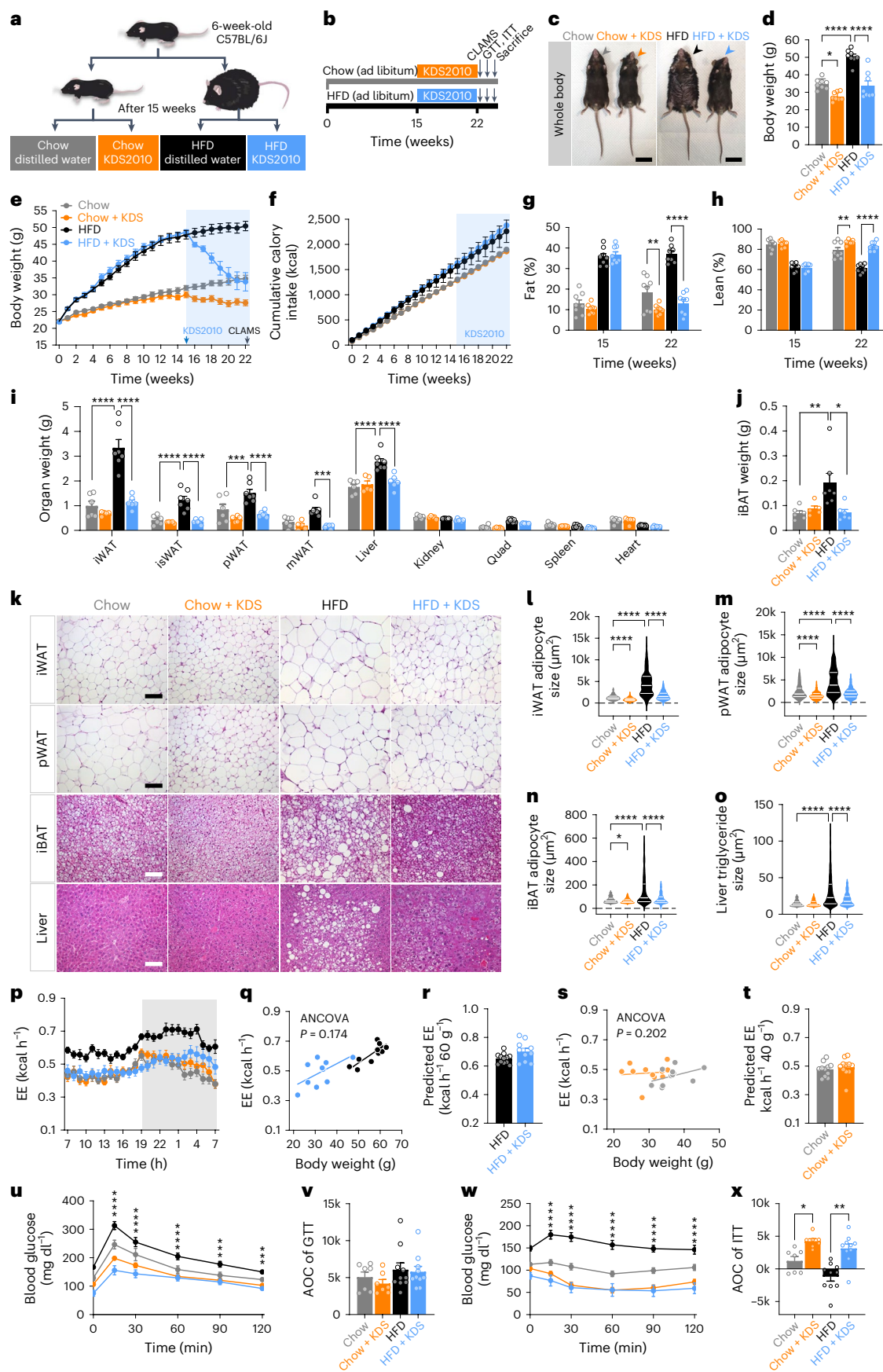
**Fig. 6 | Gene silencing of astrocytic *Maob* reduces tonic GABA in LHA.**

**a**, Scheme and timeline of whole-cell patch-clamp recording of LHA neurons in Scrambled or shMAOB groups with HFD. **b, c**, Representative traces of GABA<sub>A</sub> receptor-mediated currents recorded from Scrambled (**b**) and shMAOB (**c**). Each dot represents one cell; 50  $\mu$ M of BIC, 10  $\mu$ M of GABA were applied. **d**, GABA<sub>A</sub> receptor-mediated tonic GABA current measured from LHA cells in each group ( $n = 11$  cells from 3 mice and 7 cells from 3 mice). **e**, GABA-induced full-activation current measured from LHA neurons in each group ( $n = 11$  cells from 3 mice and 7 cells from 3 mice). **f, g**, Amplitude (**f**) and frequency (**g**) of sIPSC measured from LHA neurons in each group ( $n = 10$  cells from 3 mice and 8 cells from 3 mice). **h**, Capacitance ( $C_m$ ) of LHA neurons in each group ( $n = 11$  cells from 3 mice and 7 cells from 3 mice). **i**, Representative immunostaining for Cre (mCh), GFAP and GABA in LHA in Scrambled and shMAOB groups. Top: images of Cre; scale bars, 20  $\mu$ m. Middle: merged images of Cre, GFAP and GABA; scale bars, 20  $\mu$ m. Bottom: images of GFAP, GABA and merged overlay, taken from the boxed areas in the middle; scale bars, 10  $\mu$ m. **j**, Representative images of Sholl analysis for an astrocyte (top), and representative 3D-GFAP images from the

middle section of (**i**) for both Scrambled and shMAOB groups. **k**, The number of process intersections at each radial distance from the soma in GFAP<sup>+</sup> astrocytes in LHA ( $n = 5$  slices from 3 mice and 6 slices from 3 mice). **l**, Quantification of GFAP intensity of GFAP<sup>+</sup> astrocytes in Scrambled and shMAOB groups ( $n = 560$  cells from 3 mice and 318 cells from 3 mice). **m**, Quantification of GFAP intensity of GFAP<sup>+</sup> astrocytes in each group ( $n = 697$  cells from 3 mice and 339 cells from 3 mice). **n**, Quantification of 3D volumes of GFAP<sup>+</sup> astrocytes in each group ( $n = 207$  cells from 3 mice and 342 cells from 3 mice). **o**, Number of summarized intersections of GFAP<sup>+</sup> astrocytes in Scrambled and shMAOB groups ( $n = 336$  cells from 3 mice and 325 cells from 3 mice, respectively). **p**, Quantification of the ramification index ( $n = 334$  cells from 3 mice and 319 cells from 3 mice). **q, r**, The ending radius of GFAP<sup>+</sup> astrocytes (**q**) and the number of GFAP<sup>+</sup> astrocytes (**r**) in LHA of Scrambled and shMAOB groups ( $n = 5$  slices from 3 mice and 6 slices from 3 mice, respectively). Data are presented as mean  $\pm$  s.e.m.  $P$  values were determined by Mann–Whitney tests (**d–f, h** and **l–r**), unpaired  $t$ -test (**g**) or two-way ANOVA with Šidák's multiple comparisons (**k**). \* $P < 0.05$ , \*\* $P < 0.01$ , \*\*\* $P < 0.001$  and \*\*\*\* $P < 0.0001$ .

(Fig. 6p) were significantly decreased in the shMAOB group compared with the Scrambled group. However, the expression of GFAP (Fig. 6l), the volume (Fig. 6n), ending radius (Fig. 6q) and the number of GFAP-positive

astrocytes (Fig. 6r) were not significantly changed. Taken together, these results indicate that astrocyte-specific gene silencing of *Maob* reduces astrogliosis and tonic GABA inhibition in LHA.



### Reducing GABA production via Maob reduces obesity

Finally, we investigated whether the inhibition of astrocytic GABA synthesis in the DIO mice can decrease body weight. To test this hypothesis,

we fed HFD to 6-week-old C57BL/6J mice for 15 weeks till they reached near 50 g in body weight, after which they were treated with a recently developed highly selective and reversible Maob inhibitor, KDS2010

**Fig. 7 | Reducing GABA production via Maob reduces obesity.** **a**, Four groups of different diets with drug treatment: chow diet with distilled water, chow diet with KDS2010, HFD with distilled water and HFD with KDS2010. **b**, Experimental timeline. **c**, Representative images of a mouse from each group before killing. Scale bar, 3 cm. **d**, The average body weight of the four groups ( $n = 8$  mice per group). **e**, Curves representing the kinetics of change in body weight among chow, chow with KDS2010, HFD and HFD with KDS2010 mice over the 22 weeks of HFD treatment. The light-blue shaded box indicates the duration of KDS2010 treatment ( $n = 8$  mice per group). **f**, Cumulative food intake in chow, chow with KDS2010, HFD and HFD with KDS2010 mice over the 22 weeks of observation ( $n = 8$  mice per group). **g, h**, Quantification of percentage change of fat mass (**g**) and lean mass (**h**) before (at 15 weeks) and after (at 22 weeks) KDS2010 treatment. **i, j**, Quantification of organ weight (**i**) and average weight of iBAT (**j**) of chow, chow with KDS2010, HFD and HFD with KDS2010 group ( $n = 6, 5, 7$  and 6 mice, respectively). **k**, Representative H&E images of iWAT, pWAT, iBAT and liver. Scale bar, 100  $\mu\text{m}$ . **l–o**, Quantified adipose size of iWAT ( $n = 388, 488, 208$  and 319 cells) (**l**), pWAT ( $n = 244, 296, 176$  and 254 cells) (**m**), iBAT ( $n = 561, 394, 417$  and 439 cells) (**n**) and liver ( $n = 508, 371, 1,238$  and 677 cells) (**o**) of chow, chow with KDS2010, HFD and HFD with KDS2010 groups ( $n = 6, 5, 7$  and 6 mice,

respectively). **p**, Real-time monitoring curve in chow, chow with KDS2010, HFD and HFD with KDS2010 mice ( $n = 11, 11, 12$  and 10, respectively). **q**, Regression of EE with body weight in HFD and KDS2010-treated HFD mice ( $n = 12$  and 10 mice, respectively). **r**, Predicted EE with 60 g body weight for each individual mouse, calculated by regression lines ( $n = 12$  and 10 mice, respectively). **s**, Regression of EE with body weight in chow and KDS2010-treated chow mice ( $n = 11$  mice per group). **t**, Predicted EE with 40 g body weight for each individual mouse, calculated by regression lines ( $n = 11$  mice per group). **u**, Time course of blood glucose levels during the GTT of chow, chow with KDS2010, HFD and HFD with KDS2010 mice ( $n = 7, 7, 10$  and 10 mice, respectively). **v**, Quantification of AOC of GTT. **w**, Time course of blood glucose levels during the ITT of chow, chow with KDS2010, HFD and HFD with KDS2010 mice ( $n = 7, 7, 10$  and 10 mice, respectively). **x**, Quantification of AOC of the ITT. Data are presented as mean  $\pm$  s.e.m. *P* values were determined by one-way ANOVA with Tukey's multiple comparisons tests (**d, v** and **x**), two-way ANOVA with Šidák's multiple comparisons (**g–i**), Kruskal–Wallis tests (**j, l–o, v** and **x**), two-sided regression-based ANCOVA (**q** and **s**), two-tailed Mann–Whitney tests (**r** and **t**) or two-way ANOVA with Tukey's multiple comparisons test (**u** and **w**). \**P* < 0.05, \*\**P* < 0.01, \*\*\**P* < 0.001 and \*\*\*\**P* < 0.0001.

(ref. 65) (Fig. 7a,b). We measured body weight (Fig. 7c–e) and food intake (Fig. 7f) of chow, KDS2010-treated chow, HFD and KDS2010-treated HFD mice every week. We observed a significant and drastic decrease in body weight in KDS2010-treated HFD mice to the level of chow mice within 8 weeks (Fig. 7e) without any change in their food intake (Fig. 7f). In contrast, administration of an irreversible Maob inhibitor, selegiline, showed only a transient reduction in the body weight (Extended Data Fig. 7a–d). We then examined the body composition of each group using an EchoMRI for measurement of fat and lean mass. There was a significant reduction only in fat mass (Fig. 7g), but an increase in lean mass (Fig. 7h). These results implicate that fat-specific weight loss is due to the Maob inhibition by a reversible Maob inhibitor in the brain.

Consistent with the fat mass reduction, we observed that the weights of iWAT, isWAT, pWAT and iBAT in KDS2010-treated HFD mice (Extended Data Fig. 7e) were significantly reduced compared with that of chow mice (Fig. 7i,j). In addition to the reduction of fat mass, KDS2010 also reduced the weight of liver, which was increased by long-term treatment of HFD (Fig. 7i). Further, we examined the tissues at the cellular level using H&E staining. Consistent with the weight of each organ, histology of iWAT, pWAT and iBAT revealed a significantly reduced size of white adipocytes in KDS2010-treated HFD mice compared with HFD mice (Fig. 7k–n). Previous studies have shown that HFD induces non-alcoholic fatty liver disease<sup>66</sup>. There was a significant increase in triglycerides in the liver in HFD mice, similar to the phenotype of fatty liver, which was significantly reduced in KDS2010-treated

HFD mice (Fig. 7o). Taken together, pharmacological inhibition of Maob with KDS2010 effectively and rapidly reduces obesity without affecting food intake.

To determine whether pharmacological Maob inhibition can promote EE, we measured metabolic parameters using CLAMS. KDS2010-treated HFD mice showed no significant change in EE (Fig. 7p–t) or locomotor activity (Extended Data Fig. 7f–h) compared with HFD mice. Furthermore, we observed that KDS2010-treated HFD mice showed significantly improved glucose level at every time point (Fig. 7u) but no significant difference in glucose tolerance (Fig. 7v) compared with HFD mice. KDS2010-treated HFD mice also showed significantly improved insulin sensitivity compared with HFD mice, which exhibited symptoms of insulin resistance (Fig. 7w,x). Overall, these results imply that pharmacological inhibition of Maob leads to a body weight decrease with improved insulin sensitivity, without compromising appetite or affecting EE.

### A reversible Maob inhibitor restores decreased activity

We investigated whether GABRA5<sup>LHA</sup> are tonically inhibited in HFD mice after administration of KDS2010. To test this possibility, we performed whole-cell patch-clamp recordings in the acutely prepared LHA slices (Fig. 8a). HFD mice showed a significant increase of tonic GABA current compared with chow mice, which was reduced by KDS2010 treatment (Fig. 8b–f). There was no significant difference in the GABA-induced full-activation current, which was induced by 10  $\mu\text{M}$  GABA (Fig. 8g).

### Fig. 8 | A reversible Maob inhibitor reduces tonic GABA and restores decreased activity in LHA.

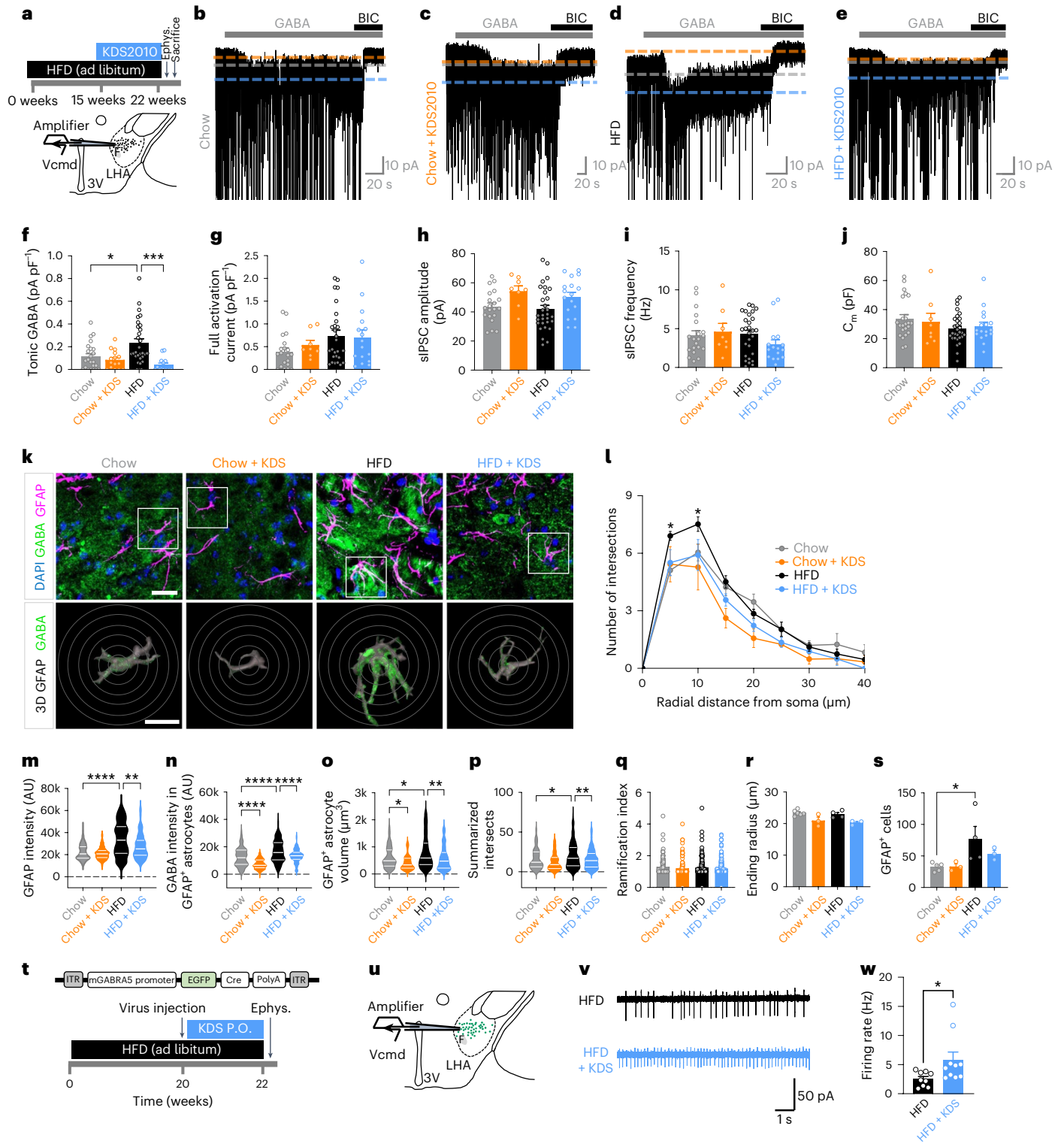
**a**, Scheme of whole-cell patch-clamp recording in LHA neurons. **b–e**, Representative traces of GABA<sub>A</sub> receptor-mediated currents recorded from chow diet (**b**), KDS2010-treated chow diet (**c**), HFD (**d**) and KDS2010-treated HFD (**e**). **f**, GABA<sub>A</sub> receptor-mediated tonic GABA current measured from LHA cells in each group: 50  $\mu\text{M}$  of BIC, 10  $\mu\text{M}$  of GABA were applied ( $n = 23, 15, 30$  and 14 cells from 6, 3, 8 and 3 mice, respectively). **g**, GABA-induced full-activation current measured from LHA neurons in each group ( $n = 20, 8, 27$  and 16 cells from 6, 3, 8 and 3 mice, respectively). **h, i**, Frequency ( $n = 20, 8, 30$  and 17 cells) (**h**) and amplitude ( $n = 20, 8, 28$  and 16 cells) (**i**) of sIPSC measured from LHA neurons in each group ( $n = 6, 3, 8$  and 3 mice, respectively). **j**, Capacitance of LHA neurons in each group ( $n = 23, 8, 30$  and 17 cells from 6, 3, 8 and 3 mice, respectively). **k**, Representative immunostaining images for GABA (green) and GFAP (magenta) in LHA of chow, chow with KDS2010, HFD and HFD with KDS2010 groups (top). Scale bar, 20  $\mu\text{m}$ . Magnified images taken from the boxed areas in the top images with 3D-rendering, showing GFAP colocalized with GABA immunostaining (bottom). Scale bar, 10  $\mu\text{m}$ . **l**, The number of process intersections at each radial distance from soma in GFAP<sup>+</sup> astrocytes in each group ( $n = 6, 3, 4$  and 3 slices from 6, 3, 4 and 3 mice, respectively). **m, n**, Quantification of GFAP intensity ( $n = 438,$

222, 248 and 112 cells, respectively) (**m**) and GABA intensity ( $n = 104, 91, 130$  and 113 cells, respectively) (**n**) in GFAP<sup>+</sup> astrocytes in each group ( $n = 6, 3, 4$  and 3 mice per group, respectively). **o–q**, Quantification for 3D volumes ( $n = 89, 69, 166$  and 117 cells, respectively) (**o**), the number of summarized intersections ( $n = 128, 94, 169$  and 205 cells, respectively) (**p**) and quantification of the ramification index ( $n = 98, 100, 173, 211$  cells, respectively) (**q**) in GFAP<sup>+</sup> astrocytes in each group ( $n = 6, 3, 4$  and 3 mice per group, respectively). **r, s**, The ending radius (**r**) and the number (**s**) of GFAP<sup>+</sup> astrocytes in LHA ( $n = 6, 3, 4$  and 3 slices from 6, 3, 4 and 3 mice, respectively). **t**, Timeline for cell-attached patch-clamp recording in GABRA5<sup>LHA</sup> of HFD or KDS2010-treated HFD mice. KDS2010 is administered per os (P.O.). **u**, Scheme of whole-cell patch-clamp recording of LHA neurons. **v**, Representative traces of cell-attached recording in GABRA5<sup>LHA</sup> from HFD (top) and KDS2010-treated HFD (bottom). **w**, Quantification of firing rate between HFD and KDS2010-treated mice ( $n = 9$  and 10 cells, respectively, from 3 mice per group). Data are presented as mean  $\pm$  s.e.m. *P* values were determined by one-way ANOVA with Tukey's multiple comparisons tests (**f–j** and **n–p**), two-way ANOVA with Šidák's multiple comparisons (**l**), one-way ANOVA with Kruskal–Wallis test (**m** and **q–s**) or Mann–Whitney test (**w**). \**P* < 0.05, \*\**P* < 0.01, \*\*\**P* < 0.001 and \*\*\*\**P* < 0.0001.

The amplitude and frequency of sIPSCs were not significantly altered, indicating that phasic or synaptic GABA was not altered (Fig. 8h,i). The capacitance of LHA neurons was not affected by HFD (Fig. 8j). These results indicate that the reversible Maob inhibitor KDS2010 significantly attenuated the tonic inhibition.

To examine the reactivity of astrocytes and astrocytic GABA levels after KDS2010 treatment, we performed immunostaining in LHA. We observed that GFAP signals (Fig. 8k,m) and GFAP-positive astrocyte volume (Fig. 8o) were significantly reduced in the LHA of KDS2010-treated HFD mice compared with HFD mice. Sholl analysis

of individual astrocytes (Fig. 8k,l) also showed that the summation of intersects (Fig. 8p) and ending radius (Fig. 8r) were significantly reduced, although the ramification index (Fig. 8q) and the number of the GFAP-positive cells (Fig. 8s) were not changed in KDS2010-treated HFD mice compared with HFD mice. As expected, we observed that Maob expression in astrocytes was significantly reduced in the LHA of KDS2010-treated HFD mice compared with HFD mice (Extended Data Fig. 7i,j). We also observed that the astrocytic GABA signals were significantly reduced in KDS2010-treated HFD mice compared with those in HFD mice (Fig. 8n). In contrast to KDS2010 (ref. 65), KDS1524



is a Maob inhibitor that hardly crosses the blood–brain barrier (BBB) (Extended Data Fig. 8a–c). As a result, KDS1524 did not reduce the increased astrocytic GABA and astrocytic reactivity in LHA (Extended Data Fig. 8g–o) but slightly reduced the body weight (Extended Data Fig. 8d–f). These effects by KDS2010 appear to be mainly through Maob inhibition in the brain rather than the peripheral system. To investigate the administration of KDS2010 changes to the firing rate in GABRA5<sup>LHA</sup>, we performed loose cell-attached patch clamping on GABRA5<sup>LHA</sup> in acutely prepared LHA slices from KDS2010-treated HFD mice (Fig. 8t,u). We found that the GABRA5<sup>LHA</sup> pacemaker firing rate was significantly restored in KDS2010-treated HFD mice (Fig. 8v,w). Taken together, these results indicate that Maob inhibition by the reversible inhibitor KDS2010 reduces astrocytic reactivity and GABA levels in LHA, thereby attenuating tonic inhibition and restoring the firing rate of GABRA5<sup>LHA</sup> in HFD mice.

## Discussion

In the present study, we have discovered the existence of a unique population of fat-burning neurons in LHA. These neurons uniquely express the high-affinity extrasynaptic GABA<sub>A</sub> receptor containing the GABRA5 subunit and are also GABA producing, that is, GABAergic GABRA5<sup>LHA</sup> (Fig. 1). Although GABAergic, these neurons appear to be projection neurons, projecting polysynaptically to iBAT and iWAT (Fig. 3). These neurons show unique electrical properties of low-threshold spiking and pacemaker firing at a firing frequency of around 5 Hz (Fig. 1). The presence of the high-affinity GABRA5 subunit allows sensing of tonically released low concentrations of extrasynaptic GABA, which has been recently characterized to be synthesized by Maob and released by reactive astrocytes under pathological conditions such as in AD and Parkinson's disease<sup>45,65</sup>. Our study unveils a causal relationship between reactive astrocytes and thermogenesis/fat storage in DIO mouse model via the complex GABA signalling in LHA. On the basis of our findings, we propose that an increase in astrocytic tonic GABA causes activation of neuronal GABA<sub>A</sub> receptors containing the  $\alpha 5$  subunit, which leads to a reduction in pacemaker firing in GABRA5<sup>LHA</sup>, attenuation of thermogenesis and augmentation of fat storage in peripheral adipose tissues (Extended Data Fig. 9). This cascade of events in the DIO model can be observed by activation of Gi-DREADD expressed in GABRA5<sup>LHA</sup> and reversed by pharmacological inhibition or gene silencing of *Maob* to reduce astrocytic GABA, as well as by gene silencing of *Gabra5* to reduce tonic GABA-induced inhibition in GABRA5<sup>LHA</sup> (Extended Data Fig. 9). Strikingly, this reversal of DIO can be achieved without compromising appetite. Our study highlights the pathological role of glia–neuron interactions via astrocytic GABA and neuronal GABRA5 in LHA and its contribution to thermogenesis/fat storage and DIO with minimal contribution to food intake.

Recent research highlights that the LHA lacks inhibitory interneurons with locally ramifying axons<sup>67</sup>. This suggests that the GABAergic neurons in the LHA project to regions outside LHA rather than locally inhibit the nearby neurons. The LHA contains a large number of GABAergic neurons expressing GAD65, GAD67 and vesicular GABA transporter<sup>19,24,68–70</sup>. These neurons are likely to be highly diverse and subdivided into many subpopulations with distinct characteristics and functions. In the current study, we have identified that GABAergic GABRA5<sup>LHA</sup> project to outside LHA and polysynaptically innervate peripheral adipose tissue, iBAT and iWAT. LHA regulates both thermogenesis and lipolysis in brown adipocytes through the sympathetic nervous system<sup>8,54,71,72</sup>. LHA also regulates lipolysis of iWAT through the sympathetic nervous system<sup>54,72,73</sup>. Intriguingly, iBAT- and iWAT-projecting neurons were heterogeneously distributed in the medial and central parts of LHA, where HFD-induced reactive astrocytes also displayed robust GFAP expression. These findings imply that HFD-induced astrocytic GABA tonically inhibits iBAT- and iWAT-projecting GABRA5<sup>LHA</sup> in the medial and central parts of the LHA. Inhibited GABRA5<sup>LHA</sup> thereby attenuate BAT thermogenesis and

suppression of fat accumulation. It has been reported that in mice injected with PRV into iBAT, PRV-infected neurons in LHA overlap with MCH and orexin<sup>74</sup>. However, there still remains an undefined population of LHA neurons that innervate both iBAT and iWAT. We propose that the GABAergic GABRA5<sup>LHA</sup> constitute a part of this remaining population. In previous studies, orexin neurons in LHA were shown to project to rostral RPa (rRPa) in the brainstem<sup>8,14</sup>, which is known to house sympathetic premotor neurons to control sympathetic output and activate iBAT<sup>75</sup>. Consistently, viral tracing evidence further demonstrates that sympathetic nerves that innervate subcutaneous WAT originate from rRPa<sup>76</sup>, which then project to sympathetic preganglionic neurons in the spinal intermediolateral nucleus<sup>77</sup>. Our results from the tissue clearing and light-sheet microscopic images suggest that GABAergic GABRA5<sup>LHA</sup> might project to PAG before reaching to rRPa (Extended Data Fig. 4). We propose that GABAergic GABRA5<sup>LHA</sup>, just like orexin neurons in LHA, may also project to rRPa, possibly after passing through PAG, and innervate iBAT and iWAT through the intermediolateral nucleus and sympathetic ganglion. Future investigations are needed to determine the exact polysynaptic circuits for GABAergic GABRA5<sup>LHA</sup> projecting to iBAT and iWAT.

Our study sheds light on the missing link between the reactive astrogliosis and obesity, delineating the molecular and cellular mechanisms of how Maob-dependent production of GABA leads to inhibition of thermogenesis and facilitation of fat storage. Elevated activity of Maob and elevated levels of Maob-dependent GABA released via BEST1 have been highly implicated in the reactive astrocytes that are found in various neuroinflammatory diseases such as AD, Parkinson's disease, epileptic seizure, a stab-wound injury model and inflammation-induced anxiety<sup>45,78–81</sup>. The growing list of reports all point to a common molecular mechanism of how resting astrocytes transform into reactive astrocytes via the putrescine-degradation pathway involving Maob under the conditions of aversive stimulations such as toxin challenges and viral infections, which usually accompany neuroinflammation<sup>28</sup>. In the current study, we report the presence of the common molecular mechanism of reactive gliosis at work in LHA to cause the production of GABA in a Maob-dependent fashion. Interestingly, we have previously reported the hypertrophy of astrocytes with elevated GABA content in ARC after chronic HFD feeding<sup>82</sup>, as in LHA. Unexpectedly, we observed that the increased astrocytic GABA synthesis was compensated by increased GABA clearance by GAT1, leaving the tonic GABA inhibition unaltered in ARC. These results suggest that the level of tonic inhibition in LHA may play a critical role in maintaining the established obesity. What then could be the toxin that turns on this mechanism in LHA? It has been reported that chronic HFD induces hypothalamic inflammation, which is associated with reactive astrocytes in the hypothalamus<sup>2</sup>, raising the possibility that the high-fat nutrition itself could be the trigger for reactive gliosis and GABA production. Indeed, we have previously reported that astrocytes in culture start to produce GABA when challenged with elevated levels of fatty acids<sup>83</sup>. Consistent with our findings, it has been reported that after chronic over-nutrition, levels of extracellular neurotransmitters such as GABA become elevated in the mediobasal hypothalamus<sup>27</sup>. In this study, we have further demonstrated that the Maob-dependent astrocytic tonic GABA induces a strong neuronal inhibition in GABRA5<sup>LHA</sup>. Interestingly, a recent study has reported astrocytic calcium activity in the hypothalamus of obese mice<sup>84</sup>. The astrocytic calcium activity was significantly increased in PVN and ARC, but not the ventromedial hypothalamus. On the basis of these findings, it is possible that LHA may also have increased astrocytic calcium activity in obese mice and may induce more tonic GABA release via increasing activity of the Best1 channel<sup>64</sup>. These possibilities need to be investigated in the future. In addition to Maob-dependent GABA, Maob-dependent H<sub>2</sub>O<sub>2</sub> has been recently implicated in neurodegeneration and brain atrophy in AD<sup>85</sup>. In line with this, we expect that the reactive astrocytes in LHA would produce excess amount of toxic H<sub>2</sub>O<sub>2</sub> in a Maob-dependent fashion,

further exacerbating the reactive astrogliosis. The excessive toxic  $H_2O_2$  would cause neuronal death on neighbouring neurons in LHA under a chronic obesity condition. Indeed, consumption of dietary fats induce apoptosis of neurons and a reduction of synaptic inputs in LHA<sup>42</sup>. This possibility of  $H_2O_2$ -induced neurodegeneration in LHA awaits future investigation.

Our study contributes an additional dimension to the existing anti-obesity drugs. It has been reported in previous studies that drugs for weight loss have a significant history of safety risks, including cardiovascular and psychiatric complications<sup>86,87</sup>. Most of the obesity drugs that target neurons in the hypothalamus are known to suppress appetite<sup>86</sup>. On the basis of our study, we identify that selective inhibition of Maob as a potential molecular target for treating obesity while overcoming the limitations of neuron-target obesity drugs. By using three pharmacological inhibitors, KDS2010, KDS1524 and selegiline, with differential properties, we have gained useful insights about designing effective therapeutic strategies. Comparison between irreversible inhibitor selegiline and reversible inhibitor KDS2010 showed that KDS2010 had long-lasting effects compared with selegiline, implying that reversibility of the Maob inhibitor is critical for long-lasting efficacy. These results are consistent with our previous reports on the superior effect of reversible Maob inhibitors on animal models of AD and Parkinson's disease<sup>65,80</sup>. Furthermore, the BBB-permeable KDS2010 was more efficient in maintaining body weight as compared with the less BBB-permeable KDS1524 (Extended Data Fig. 8), implying that Maob in the brain is a better target for developing anti-obesity drugs than the peripheral Maob. Inhibition of Maob can also affect other organs or other hypothalamic regions, such as ARC and the paraventricular hypothalamus, where reactive astrocytes are readily observed after HFD<sup>41</sup>, which could account for the rapid effect of KDS2010 administration on weight loss after HFD (Fig. 7 and Extended Data Fig. 8). KDS2010 treatment could also be ameliorating reactive astrogliosis and aberrant tonic GABA inhibition throughout various hypothalamic regions, thus eliminating the undesirable inhibition of neuronal activity. It would be interesting to investigate the existence and physiological roles of GABRA5-positive neurons in other hypothalamic regions. We, therefore, conclude that Maob-mediated GABA in the whole brain may play a causative role in obesity, evidenced by the complete elimination of obesity through pharmacological inhibition of Maob by KDS2010 (Fig. 7). In contrast, the astrocytic Maob-mediated GABA in LHA is critical for maintaining established obesity, evidenced by the reduced body weight at 8 weeks after gene silencing of *Maob* (Fig. 5). The difference in the long-term efficacy between selegiline and KDS2010 (Extended Data Fig. 7) has been mechanistically explained by how reversible and irreversible inhibitors differentially act on the Maob enzyme; irreversible inhibitors such as selegiline covalently modify the Maob enzyme and destroy the enzyme itself to turn on the compensatory expression of enzyme diamine oxidase, which continues to produce GABA, whereas reversible inhibitors occupy the active site of Maob competitively, resulting in an intact Maob enzyme with no compensatory mechanism<sup>65</sup>. Importantly, both reversible and irreversible selective inhibition of Maob does not affect food intake and appetite. These distinctive features of Maob inhibitors will help in the development of improved anti-obesity drugs in the future.

While our study provides valuable insights into GABRAS<sup>LHA</sup>, reactive astrocytes and fat tissues in DIO mice, we exclusively used male mice. The incorporation of female mice would have enabled a more comprehensive understanding of the observed findings, including potential sex-specific differences or the influence of female hormonal factors. In our experimental design, we deliberately included two specific time points to capture different stages of weight gain: one representing a moderate level of weight gain and the other representing advanced or severe weight gain. The inclusion of additional time points would have facilitated a more detailed characterization of the temporal dynamics and progression of astrogliosis in relation to the

experimental conditions. Furthermore, our understanding of the role of Best1, a mechanism responsible for releasing astrocytic GABA, in the regulation of obesity is unexplored. While GABA is synthesized by Maob, Best1 serves as the secretion channel for GABA. Further investigation is warranted to fully elucidate the intricate mechanisms by which Best1-mediated GABA release contributes to the regulation of obesity. In summary, we identify GABRAS<sup>LHA</sup> as distinct GABAergic projecting and pacemaker-firing neurons that facilitate BAT thermogenesis and suppress fat accumulation in WAT. Our findings establish the GABRAS<sup>LHA</sup> as key players involved in the astrocyte–neuron interaction mediated by GABA in the hypothalamus of a DIO mouse model. Our study raises promising molecular targets to combat obesity without compromising appetite.

## Methods

### Animals and housing

All animal experiments were performed according to procedures approved by the Institutional Animal Care and Use Committee of the Institute for Basic Science (IBS; Daejeon, Republic of Korea) and Korea Institute of Science and Technology (KIST; Seoul, Republic of Korea). All mice were maintained in a specific pathogen-free controlled animal facility. These conditions included a 12 h light–dark cycle with lights on at 8:00 AM at a temperature of 21 °C, and a humidity range of 40–60%. The mice were allowed free access to water and food. All experiments on the DIO mouse model were conducted using the C57BL/6J background from either the Jackson Laboratory (USA, stock number 000664) or DBL (Republic of Korea). Six-week-old male C57BL/6J mice were fed a HFD (60% kcal fat, D12492, Research Diets Inc.) or chow (Teklad, 2018S, Envigo) for ~6–23 weeks. All experiments were done with age-matched controls.

### Stereotaxic injection

Mice were anaesthetized using isoflurane anaesthesia (induction 3–4% and maintenance 1.5–2%) and placed into stereotaxic frames (Kopf). The scalp was incised and a hole was drilled into the skull above the LHA (anterior/posterior, –1.58 mm; medial/lateral, –1.0 or +1.0 mm from bregma). Coordinates were identified using the Allen mouse brain atlas. For characterization studies, C57BL/6J mice were injected with 1.0  $\mu$ l of AAV–mGABRA5–EGFP–cre virus on both sides of the LHA. For GABRA5 knockdown studies, C57BL/6J mice were injected with 1.0  $\mu$ l of Lenti–pSicoR–GABRA5–shRNA–mCherry or Lenti–Scrambled–mCherry virus on both sides of the LHA. For chemogenetic studies, AAV5–mGABRA5–EGFP–Cre with AAV5–hSyn–DIO–hM4Di–mCherry (inhibition) or AAV5–hSyn–DIO–mCherry (control virus) were injected on both sides of the LHA. For astrocyte-specific Maob knockdown studies, AAV–GFAP–Cre–mCherry with Lenti–pSico–Scrambled–GFP or Lenti–pSico–shMAOB–GFP virus were used on both sides of the LHA. The virus was loaded into a stainless needle and injected bilaterally into the LHA (dorsal/ventral, –5.0 mm) at a rate of 0.1  $\mu$ l  $\text{min}^{-1}$  for 10 min using a syringe pump (KD Scientific). At the end of the infusion, the needle was left in the brain for another 10 min to reduce backflow of the virus. Shortly after surgery, mice were translocated to their home cages.

### Slice preparation for electrophysiology

Mice were deeply anaesthetized with vapourized isoflurane and then decapitated to isolate the brain. The isolated brains were quickly excised from the skull and submerged in ice-cold *N*-methyl-D-glucamine (NMDG) recovery solution containing 93 mM *N*-methyl-D-glucamine, 93 mM HCl, 30 mM  $\text{NaHCO}_3$ , 20 mM HEPES, 25 mM glucose, 5 mM sodium ascorbate, 2.5 mM KCl and 1.2 mM  $\text{NaH}_2\text{PO}_4$  (pH 7.4.). All the solution was gassed with 95%  $\text{O}_2$  and 5%  $\text{CO}_2$ . The brain was glued onto the stage of a vibrating microtome (Linear Slicer Pro7, D.S.K.) and 250- $\mu$ m-thick coronal slices were prepared. For stabilization, slices were incubated in room temperature for at least 1 h in extracellular artificial cerebrospinal fluid (aCSF) solution containing 130 mM NaCl,

3.5 mM KCl, 24 mM NaHCO<sub>3</sub>, 1.25 mM NaH<sub>2</sub>PO<sub>4</sub>, 1.5 mM CaCl<sub>2</sub>, 1.5 mM MgCl<sub>2</sub> and 10 mM D-(+)-glucose, pH 7.4, and simultaneously equilibrated at 25 °C. Slices were transferred to a recording chamber that was continuously perfused with aCSF solution.

### Patch-clamp recording

For the characterization of GABRA5<sup>LHA</sup> cells, electrophysiological experiments were conducted with reference to a previous study<sup>19</sup>. Patch electrodes (4–8 MΩ) were filled with an intrapipette solution containing 120 mM potassium gluconate, 10 mM KCl, 1 mM MgCl<sub>2</sub>, 0.5 mM ethyleneglycol bis(2-aminoethyl ether)-*N,N,N',N'* tetraacetic acid (EGTA), and 40 mM HEPES (pH 7.2 adjusted with KOH). Resting membrane potential (mV) was measured at  $I = 0$  soon after membrane rupture. Step current was injected in current clamp mode to measure maximum firing frequency (Hz), which is the reciprocal of the average of the first four peak intervals (ISI) calculated after the highest injected current before the occurrence of spike inactivation. The spike ratio was determined by calculating  $X/(Y/2)$  from the number of spikes before (500 ms window,  $Y$ ) and after (250 ms window,  $X$ ) hyperpolarization by the negative current step. Classification of cells, which is late spiking for <0.5, regular spiking for between 0.5 and 1.5 and low-threshold spiking for >1.5, followed a previous study<sup>19</sup>. For the measurement of spontaneous spike activity in GABRA5<sup>LHA</sup>, a cell-attached patch was conducted as previously described<sup>88</sup>. Patch electrodes (4–8 MΩ) were filled with normal aCSF solution. The slice chamber was mounted on the stage of an upright microscope and viewed with a 60× water immersion objective (numerical aperture 0.90) with infra-red differential interference contrast optics. Cellular morphology was visualized by a complementary metal oxide semiconductor camera and the Imaging Workbench software (INDEC BioSystems, ver. 9.0.4.0.).

### Tonic GABA recording

Whole-cell patch-clamp recording was conducted as previously described<sup>45</sup>. The holding potential was –60 mV. Pipette resistance was typically 6–8 MΩ and the pipette was filled with an internal solution consisting of 135 mM CsCl, 4 mM NaCl, 0.5 mM CaCl<sub>2</sub>, 10 mM HEPES, 5 mM ethyleneglycol bis(2-aminoethyl ether)-*N,N,N',N'* tetraacetic acid, 2 mM Mg-ATP, 0.5 mM of Na<sub>2</sub>-GTP and 10 mM of QX-314, pH-adjusted to 7.2 with CsOH (278–285 mOsmol). Before measuring the tonic current, the baseline current was stabilized with D-AP5 (50 μM) and CNQX (20 μM) to isolate GABA<sub>A</sub> receptor current from the AMPAR and NMDAR. Electrical signals were digitized and sampled at 10 ms intervals with the Digidata 1550 data acquisition system and the Multiclamp 700B Amplifier (Molecular Devices) using pClamp10.2 software. Data were filtered at 2 kHz. The amplitude of the tonic GABA current was measured by the baseline shift in response to the bath application of bicuculline (50 μM) using Clampfit software (ver. 10.6.0.13.). The frequency and amplitude of spontaneous inhibitory post-synaptic currents before BIC administration was detected and measured by Mini Analysis (Synaptosoft, ver. 6.0.7.)

### Immunohistochemistry

Mice were deeply anaesthetized with isoflurane and transcardially perfused with 0.9% saline followed by ice-cold 4% paraformaldehyde. Excised brains were postfixed overnight at 4 °C and transferred to 30% sucrose for 48 h and cut with a frozen microtome in coronal 30 μm sections. Brain sections were translocated into 24-well plates filled with blocking solution (0.3% Triton X-100 and 3% Donkey Serum in 0.1 M phosphate-buffered saline (PBS)). Primary antibodies were added to blocking solution at desired dilution and slices were incubated in a shaker at 4 °C overnight. Primary antibodies for immunostaining were anti-GABRA5 (rabbit, 1:500), Orexin A (rabbit, 1:100), Orexin B (rabbit, 1:500), MCH (rabbit, 1:200), GABA (rabbit, 1:200), GFAP (chicken, 1:500), S100β (rabbit, 1:200), Maob (mouse, 1:100), NeuN (mouse or guinea pig, 1:500) and c-FOS (rabbit, 1:500). Antibody details can be

found in the Supplementary Table 1. Unbound antibodies were washed off using PBS, followed by corresponding secondary antibody incubation (in blocking solution) for 1 or 2 h at room temperature. Unbound antibodies were washed with PBS and 4,6-diamidino-2-phenylindole (DAPI) was added to PBS (1:1,500 dilution) in the second step to visualize the nuclei of the cells. Sections were mounted with fluorescent mounting medium (Dako) and dried. A series of fluorescent images was obtained by a Zeiss LSM900 confocal microscope using a 20x, 40x or 63x objectives. Z stack images were processed using the ZEN Digital Imaging for Light Microscopy blue system (Zeiss, ver. 3.2) and ImageJ (NIH, ver. 1.52s.) software.

### Image quantification

Confocal microscopic images were obtained to quantify the number of colocalized cells, and the expression was analysed using the ImageJ (NIH) program. Fluorescence intensities were calculated by determining the mean intensity value of each fluorescence pixel in the marker-positive area. The marker-positive area was defined by thresholding and converted into a binary mask. The mean intensity of immunostained pixels in the binary mask was then calculated. Sholl analysis was performed on serially stacked and maximally projected confocal images over 20 μm stacks, as previously described<sup>89</sup>. Confocal images of brain sections immunostained with the GFAP antibody were used for Sholl analysis. The Sholl analysis plugin, applied in IMARIS software (version 9.0.1, Oxford Instruments) constructs serially concentric circles at 10 μm intervals from the centre of the GFAP signal (soma) to the end of the most distal process of each astrocyte. The number of intercepts of GFAP-positive processes at each circle and the radius of the largest circle intercepting the astrocyte are then analysed. To measure the GFAP-positive volume of astrocytes, the GFAP signals were reconstructed into a 3D object using IMARIS software (version 9.0.1, Oxford Instruments).

### Tissue isolation and histological analysis

Mice were deeply anaesthetized with isoflurane, and the organs were immediately isolated from the mice bodies. We isolated inguinal WAT (iWAT), interscapular WAT (isWAT), perigonadal WAT (pWAT), mesenteric WAT (mWAT), liver, quad muscle, kidney, spleen and heart. After measuring the weight of each organ, iBAT, iWAT, pWAT and liver tissues were fixed with 4% paraformaldehyde (Sigma-Aldrich) overnight and then conducted further processes. Histological changes of lipid droplets were examined by H&E staining. As a counterstain, Mayer's hematoxylin was used for every slide. H&E images were obtained with an Eclipse TI-E microscope and analysed using the ImageJ (NIH) program.

### Tissue clearing and light-sheet imaging

Mice underwent transcardial perfusion with ice-cold PBS followed by the SHIELD perfusion solution (Passive clearing, Lifecanvas, 500 ml kit, cat. no. PCK-500), as described previously<sup>90</sup>. The dissected brains were then immersed in the same perfusion solution and kept at 4 °C for 48 h. Subsequently, they were transferred to the SHIELD-OFF solution and incubated at 4 °C for 24 h. After that, the brains were placed in the SHIELD-ON solution and incubated at 37 °C for 24 h. The SHIELD-fixed brains were passively cleared for a few weeks (10–14 days at 45 °C for a mouse brain hemisphere) in a buffer solution. Once the tissues were delipidated, they were incubated in Protos-based immersion media until the tissue became transparent without any visible haze at the tissue–medium interface. Finally, 3D light-sheet images were captured using Zeiss Light sheet Fluorescence microscopy.

### Metabolic analysis

For metabolic analysis, mice were measured using the CLAMS (Columbus Instruments, PhenoMaster, TSE systems). All mice for metabolic analysis were maintained in an animal facility under a 12 h light–dark cycle (lights on at 7:00 AM) at a temperature of 21 °C and



allowed free access to water and food. The mice were individually acclimated to the metabolic chamber cage before measuring EE for at least 3 days, and then data were collected from days 3–5 and analysed. Using direct calorimetry, EE was assessed by the direct measurement of the body's heat production in a calorimeter<sup>91</sup>. Then, the EE data were analysed by ANCOVA using body weight as a covariant, as previously described<sup>49</sup>. The ANCOVA analysis for EE was analysed using MedCalc software (ver. 20.218), which could discriminate between mass-dependent and mass-independent EE. The predicted EE at body weight was calculated using the regression line equation,  $y = ax + b$ . For the glucose tolerance test (GTT), mice were fasted overnight (18 h) before intraperitoneal injection of D-glucose (2 g kg<sup>-1</sup> body weight). Subsequently, the clearance of plasma glucose was monitored following glucose administration. For the insulin tolerance test (ITT), mice were fasted for 4 h before intraperitoneal injection of 0.75 U kg<sup>-1</sup> body weight of insulin for chow, KDS2010-treated chow mice, HFD and KDS2010-treated HFD mice. For all other animal models, 1 U kg<sup>-1</sup> body weight of insulin was intraperitoneally injected. All glucose levels were examined with tail-vein blood at indicated intervals (15, 30, 60, 90 and 120 min) after injection using a glucometer. After that, the areas of the curve (AOCs) for GTT and ITT were analysed as described previously<sup>92</sup>. For analysing metabolic parameters, insulin (90080, Crystal Chem) was determined. For body composition measurement, fat and lean mass of each mouse in this study were measured by an EchoMRI100V, quantitative nuclear resonance system (Echo Medical Systems).

### Temperature measurement

Temperatures of both the BAT ( $T_{BAT}$ ) and tail ( $T_{Tail}$ ) were obtained using a thermal infra-red camera (E6, Teledyne FLIR). To measure  $T_{BAT}$ , the hair on the interscapular BAT was removed 3 days before measurement and three to four images were captured from each animal.  $T_{BAT}$  was determined from the average temperature of a spherical area centred in BAT region and  $T_{Tail}$  was defined by spot measurement using FLIR software (FLIR tools, Teledyne FLIR). Data from three images in each animal were averaged and compared among groups.

### DREADD experiments

For DREADD experiments, 6–7-week-old mice were injected with either AAV-hSyn-DIO-mCherry or AAV-hSyn-DIO-hM4Di-mCherry with AAV-mGABRA5-EGFP-Cre ( $3.8 \times 10^{13}$  GC ml<sup>-1</sup>) into the lateral hypothalamus of C57BL/6J. Following a recovery period of 3 weeks, mice were given 5 mg kg<sup>-1</sup> day<sup>-1</sup> CNO in drinking and HFD food (TD 06414, Envigo) for 5 weeks to measure body weight and food consumption every week. CNO was dissolved in distilled water and protected from the light.

### RT-qPCR

RT-qPCR was carried out using SYBR Green PCR Master Mix as described previously<sup>93</sup>. Briefly, reactions were performed in triplets in a total volume of 10  $\mu$ l containing 10 pM primer, 4  $\mu$ l cDNA and 5  $\mu$ l power SYBR Green PCR Master Mix (Applied Biosystems). The mRNA level of each gene was normalized to that of 18S mRNA. Fold change was calculated using the 2<sup>- $\Delta\Delta$ CT</sup> method. The following primer sequences were used for RT-qPCR:

18S forward: 5'- TGGCTC ATAAATCAGTTATGGT -3'  
 18S reverse: 5'- GTCGGCATGTATTAGCTCTAG -3'  
 Ucp1 forward: 5'- ACTGCCACACCTCCAGTCATT -3'  
 Ucp1 reverse: 5'- CTTTGCCCTCACTCAGGATTGG -3'  
 Cidea forward: 5'- TTCAAGGCCGTGTTAAGGAATC -3'  
 Cidea reverse: 5'- CCAGGAAGTGTCCCGTCATC -3'  
 Prdm16 forward: 5'- CAGCACGGTGAAGCCATTC -3'  
 Prdm16 reverse: 5'- GCGTGCATCCGCTTGTG -3'  
 Pgc1a forward: 5'- AACCCACACCCACAGGATCAGA -3'  
 Pgc1a reverse: 5'- TCTTCGCTTTATTGCTCCATGA -3'

Dio2 forward: 5' - CCACCTGACCACCTTCTACT - 3'  
 Dio2 reverse: 5' - TGGTTCCGGTGCTTCTTAAC - 3'  
 Adrb3 forward: 5' - CGACATGTTCTCCACAAATCA - 3'  
 Adrb3 reverse: 5' - TGGATTCTGCTCTCAAACCTA ACC - 3'

### Preparation of gene-specific shRNA and shRNA virus

The shRNA sequences for Scrambled and Maob were adopted from previous studies<sup>30,94</sup>. The shRNA sequence for *Gabra5* was designed with BLOCK-iT RNAi Designer (Invitrogen) and cloned into pSicoR lentiviral vectors as previously described<sup>95</sup>. pSicoR vectors were utilized for plasmid-based shRNA expression in vitro. GABRA5 shRNA was prepared from human embryonic kidney 293T (HEK293T) cell purchased from ATCC (CRL-3216, ATCC). Cells were cultured in Dulbecco's modified Eagle medium (Gibco) supplemented with 25 mM glucose, 4 mM L-glutamine, 1 mM sodium pyruvate, 10% heat-inactivated foetal bovine serum (10082-147, Gibco) and 10,000 units ml<sup>-1</sup> penicillin-streptomycin (15140-122, Gibco). Cultures were maintained at 37 °C in a humidified atmosphere containing 95% air and 5% CO<sub>2</sub>. Cells were transfected with a DNA clone by transfection reagent (Effectene, 301425, Qiagen). Every construct was verified with sequencing after cloning. Cloned shRNA constructs were packaged into lenti viruses in the IBS Virus Facility (<http://ibs.re.kr/virusfacility>) and KIST Virus Facility (<http://virus.kist.re.kr>).

Sequence of Scrambled shRNA for control: 5'-TCGCATAGC GTATGCCGTT-3'

Antisense sequence of shRNA target for Maob: 5'-AATCGTAAGATA CGATTCTGG-3'

Antisense sequence of shRNA target for GABRA5: 5'-CTTAAACCGCA GCCTTTCATC-3'

### PRV inoculation

Recombinant PRV inoculation was performed in a biosafety level-2 operating room. For polysynaptic and retrograde circuit mapping from interscapular BAT and inguinal WAT, mice were anaesthetized with vapourized isoflurane and settled in a brain stereotaxic apparatus (RWD Life Science Co.). After the interscapular BAT or inguinal WAT were exposed, two 500 nl injections of a PRV-CAG-EGFP were made into the brown fat or white fat on one side using a Hamilton syringe (KD Scientific). Shortly after surgery, mice were translocated to their home cages. After 5 days of microinjection, the animals were deeply anaesthetized and then transcardially perfused and processed for immunohistochemistry.

### Drug administration

KDS2010, a Maob inhibitor, was synthesized as previously described<sup>65</sup>. To test the effect of KDS2010 in HFD mice, we administered KDS2010 for 7–8 weeks through dissolving the compound in drinking water. The amount of KDS2010 was calculated as 20 mg kg<sup>-1</sup> daily. Selegiline was dissolved in drinking water as calculated at 10 mg kg<sup>-1</sup> daily as previously described<sup>45</sup>. To compare the effect of KDS1524 with KDS2010, mice were orally administered 30 mg kg<sup>-1</sup> of each drug for 15 days.

### Statistics and reproducibility

All analyses were done blindly. The numbers and individual dots refer to the number of cells unless otherwise clarified in figure legends. The key findings of the paper were confirmed by multiple complementary experiments. All experiments were conducted with a sufficient number of animals that exhibited consistent effects. For data presentation and statistical analysis, GraphPad Prism (GraphPad Software) was used. For electrophysiology analysis, MiniAnalysis (synaptosoft) and Clampfit (Molecular Devices) were used. For CLAMS analysis, Oxymax for Windows software was used. For image analysis, ImageJ (NIH, ver. 1.52s.) and IMARIS (Version 9.0.1, Oxford Instruments) software were used. Statistical significance was set at \* $P < 0.05$ , \*\* $P < 0.01$ , \*\*\* $P < 0.001$  and \*\*\*\* $P < 0.0001$ .

## Reporting summary

Further information on research design is available in the Nature Portfolio Reporting Summary linked to this article.

## Data availability

The accession numbers are listed in Supplementary Table 1. The sequences of the shRNAs used in this study have been provided in the supplementary figures. The viruses used in this study were provided by and are available from the IBS Virus Facility (<https://www.ibs.re.kr/virusfacility>) and Korea Institute of Science and Technology Virus Facility upon request (<http://virus.kist.re.kr>). Microscopy data reported in this paper will be shared by the lead contact upon request. This paper does not report any original code. Any additional information required to reanalyse the data reported in this paper is available from the lead contact upon request. Source data are provided with this paper.

## References

1. Kong, D. et al. GABAergic RIP-Cre neurons in the arcuate nucleus selectively regulate energy expenditure. *Cell* **151**, 645–657 (2012).
2. Thaler, J. P. et al. Obesity is associated with hypothalamic injury in rodents and humans. *J. Clin. Invest.* **122**, 153–162 (2012).
3. Flament-Durand, J. The hypothalamus: anatomy and functions. *Acta Psychiatr. Belg.* **80**, 364–375 (1980).
4. Bernardis, L. L. & Bellinger, L. L. The lateral hypothalamic area revisited: neuroanatomy, body weight regulation, neuroendocrinology and metabolism. *Neurosci. Biobehav. Rev.* **17**, 141–193 (1993).
5. Palkovits, M., Makara, G. B., Leranthy, C. & Van Cuc, H. Intrahypothalamic terminals of stress conducting fibers. *Brain Res.* **190**, 399–407 (1980).
6. Stuber, G. D. & Wise, R. A. Lateral hypothalamic circuits for feeding and reward. *Nat. Neurosci.* **19**, 198–205 (2016).
7. Cerri, M. & Morrison, S. F. Activation of lateral hypothalamic neurons stimulates brown adipose tissue thermogenesis. *Neuroscience* **135**, 627–638 (2005).
8. Contreras, C., Nogueiras, R., Dieguez, C., Rahmouni, K. & Lopez, M. Traveling from the hypothalamus to the adipose tissue: the thermogenic pathway. *Redox Biol.* **12**, 854–863 (2017).
9. Lee, J., Raycraft, L. & Johnson, A. W. The dynamic regulation of appetitive behavior through lateral hypothalamic orexin and melanin concentrating hormone expressing cells. *Physiol. Behav.* **229**, 113234 (2021).
10. Sakurai, T. et al. Orexins and orexin receptors: a family of hypothalamic neuropeptides and G protein-coupled receptors that regulate feeding behavior. *Cell* **92**, 573–585 (1998).
11. Bittencourt, J. C. Anatomical organization of the melanin-concentrating hormone peptide family in the mammalian brain. *Gen. Comp. Endocrinol.* **172**, 185–197 (2011).
12. Oldfield, B. J. et al. The neurochemical characterisation of hypothalamic pathways projecting polysynaptically to brown adipose tissue in the rat. *Neuroscience* **110**, 515–526 (2002).
13. Berthoud, H. R., Patterson, L. M., Sutton, G. M., Morrison, C. & Zheng, H. Orexin inputs to caudal raphe neurons involved in thermal, cardiovascular, and gastrointestinal regulation. *Histochem. Cell Biol.* **123**, 147–156 (2005).
14. Tupone, D., Madden, C. J., Cano, G. & Morrison, S. F. An orexinergic projection from perifornical hypothalamus to raphe pallidus increases rat brown adipose tissue thermogenesis. *J. Neurosci.* **31**, 15944–15955 (2011).
15. Contreras, C. et al. The brain and brown fat. *Ann. Med.* **47**, 150–168 (2015).
16. Kakizaki, M. et al. Differential roles of each orexin receptor signaling in obesity. *iScience* **20**, 1–13 (2019).
17. Zink, A. N., Bunney, P. E., Holm, A. A., Billington, C. J. & Kotz, C. M. Neuromodulation of orexin neurons reduces diet-induced adiposity. *Int. J. Obes.* **42**, 737–745 (2018).
18. Kosse, C., Schone, C., Bracey, E. & Burdakov, D. Orexin-driven GAD65 network of the lateral hypothalamus sets physical activity in mice. *Proc. Natl Acad. Sci. USA* **114**, 4525–4530 (2017).
19. Karnani, M. M., Szabo, G., Erdelyi, F. & Burdakov, D. Lateral hypothalamic GAD65 neurons are spontaneously firing and distinct from orexin- and melanin-concentrating hormone neurons. *J. Physiol.* **591**, 933–953 (2013).
20. Backberg, M., Ultenius, C., Fritschy, J. M. & Meister, B. Cellular localization of GABA receptor alpha subunit immunoreactivity in the rat hypothalamus: relationship with neurones containing orexigenic or anorexigenic peptides. *J. Neuroendocrinol.* **16**, 589–604 (2004).
21. Bonnavion, P., Mickelsen, L. E., Fujita, A., de Lecea, L. & Jackson, A. C. Hubs and spokes of the lateral hypothalamus: cell types, circuits and behaviour. *J. Physiol.* **594**, 6443–6462 (2016).
22. Shin, S. Y. et al. Identification of the adrenoceptor subtypes expressed on GABAergic neurons in the anterior hypothalamic area and rostral zona incerta of GAD65-eGFP transgenic mice. *Neurosci. Lett.* **422**, 153–157 (2007).
23. Hassani, O. K., Henny, P., Lee, M. G. & Jones, B. E. GABAergic neurons intermingled with orexin and MCH neurons in the lateral hypothalamus discharge maximally during sleep. *Eur. J. Neurosci.* **32**, 448–457 (2010).
24. Jennings, J. H., Rizzi, G., Stamatakis, A. M., Ung, R. L. & Stuber, G. D. The inhibitory circuit architecture of the lateral hypothalamus orchestrates feeding. *Science* **341**, 1517–1521 (2013).
25. Jung, S. et al. A forebrain neural substrate for behavioral thermoregulation. *Neuron* **110**, 266–279.e9 (2022).
26. de Vrind, V. A. J., Rozeboom, A., Wolterink-Donselaar, I. G., Luijendijk-Berg, M. C. M. & Adan, R. A. H. Effects of GABA and leptin receptor-expressing neurons in the lateral hypothalamus on feeding, locomotion, and thermogenesis. *Obesity* **27**, 1123–1132 (2019).
27. Zhang, Y., Reichel, J. M., Han, C., Zuniga-Hertz, J. P. & Cai, D. Astrocytic process plasticity and IKK $\beta$ /NF- $\kappa$ B in central control of blood glucose, blood pressure, and body weight. *Cell Metab.* **25**, 1091–1102.e1094 (2017).
28. Chun, H. et al. Astrocytic proBDNF and tonic GABA distinguish active versus reactive astrocytes in hippocampus. *Exp. Neurol.* **27**, 155–170 (2018).
29. Chun, H. & Lee, C. J. Reactive astrocytes in Alzheimer's disease: a double-edged sword. *Neurosci. Res.* **126**, 44–52 (2018).
30. Yoon, B. E. et al. Glial GABA, synthesized by monoamine oxidase B, mediates tonic inhibition. *J. Physiol.* **592**, 4951–4968 (2014).
31. Rossi, M. A. et al. Obesity remodels activity and transcriptional state of a lateral hypothalamic brake on feeding. *Science* **364**, 1271–1274 (2019).
32. Yang, L., Qi, Y. & Yang, Y. Astrocytes control food intake by inhibiting AGRP neuron activity via adenosine A1 receptors. *Cell Rep.* **11**, 798–807 (2015).
33. Chen, N. et al. Direct modulation of GFAP-expressing glia in the arcuate nucleus bi-directionally regulates feeding. *eLife* **5**, e18716 (2016).
34. Varela, L. et al. Hunger-promoting AgRP neurons trigger an astrocyte-mediated feed-forward autoactivation loop in mice. *J. Clin. Invest.* **131**, e144239 (2021).
35. Bouyakdan, K. et al. The gliotransmitter ACBP controls feeding and energy homeostasis via the melanocortin system. *J. Clin. Invest.* **129**, 2417–2430 (2019).
36. McDougal, D. H., Hermann, G. E. & Rogers, R. C. Astrocytes in the nucleus of the solitary tract are activated by low glucose or glucoprivation: evidence for glial involvement in glucose homeostasis. *Front. Neurosci.* **7**, 249 (2013).

37. Chari, M. et al. Glucose transporter-1 in the hypothalamic glial cells mediates glucose sensing to regulate glucose production in vivo. *Diabetes* **60**, 1901–1906 (2011).
38. Kim, J. G. et al. Leptin signaling in astrocytes regulates hypothalamic neuronal circuits and feeding. *Nat. Neurosci.* **17**, 908–910 (2014).
39. Garcia-Caceres, C. et al. Astrocytic insulin signaling couples brain glucose uptake with nutrient availability. *Cell* **166**, 867–880 (2016).
40. Gonzalez-Garcia, I. & Garcia-Caceres, C. Hypothalamic astrocytes as a specialized and responsive cell population in obesity. *Int. J. Mol. Sci.* **22**, 6176 (2021).
41. Buckman, L. B., Thompson, M. M., Moreno, H. N. & Ellacott, K. L. Regional astrogliosis in the mouse hypothalamus in response to obesity. *J. Comp. Neurol.* **521**, 1322–1333 (2013).
42. Moraes, J. C. et al. High-fat diet induces apoptosis of hypothalamic neurons. *PLoS ONE* **4**, e5045 (2009).
43. Lizarbe, B., Cherix, A., Duarte, J. M. N., Cardinaux, J. R. & Gruetter, R. High-fat diet consumption alters energy metabolism in the mouse hypothalamus. *Int. J. Obes.* **43**, 1295–1304 (2019).
44. Yoon, B. E., Woo, J. & Lee, C. J. Astrocytes as GABA-ergic and GABA-ceptive cells. *Neurochem. Res.* **37**, 2474–2479 (2012).
45. Jo, S. et al. GABA from reactive astrocytes impairs memory in mouse models of Alzheimer's disease. *Nat. Med.* **20**, 886–896 (2014).
46. Brickley, S. G. & Mody, I. Extrasynaptic GABA(A) receptors: their function in the CNS and implications for disease. *Neuron* **73**, 23–34 (2012).
47. Caraiscos, V. B. et al. Tonic inhibition in mouse hippocampal CA1 pyramidal neurons is mediated by alpha5 subunit-containing gamma-aminobutyric acid type A receptors. *Proc. Natl Acad. Sci. USA* **101**, 3662–3667 (2004).
48. Hortnagl, H. et al. Patterns of mRNA and protein expression for 12 GABAA receptor subunits in the mouse brain. *Neuroscience* **236**, 345–372 (2013).
49. Muller, T. D., Klingenspor, M. & Tschope, M. H. Revisiting energy expenditure: how to correct mouse metabolic rate for body mass. *Nat. Metab.* **3**, 1134–1136 (2021).
50. Kurylowicz, A. et al. Obesity is associated with a decrease in expression but not with the hypermethylation of thermogenesis-related genes in adipose tissues. *J. Transl. Med.* **13**, 31 (2015).
51. Cero, C. et al.  $\beta$ -Adrenergic receptors regulate human brown/beige adipocyte lipolysis and thermogenesis. *JCI Insight* **6**, e139160 (2021).
52. Whittle, A. J. et al. Soluble LR11/SorLA represses thermogenesis in adipose tissue and correlates with BMI in humans. *Nat. Commun.* **6**, 8951 (2015).
53. Orozco-Solis, R. et al. The circadian clock in the ventromedial hypothalamus controls cyclic energy expenditure. *Cell Metab.* **23**, 467–478 (2016).
54. Cannon, B. & Nedergaard, J. Brown adipose tissue: function and physiological significance. *Physiol. Rev.* **84**, 277–359 (2004).
55. Cao, L. et al. White to brown fat phenotypic switch induced by genetic and environmental activation of a hypothalamic-adipocyte axis. *Cell Metab.* **14**, 324–338 (2011).
56. Grujic, D. et al.  $\beta$ -Adrenergic receptors on white and brown adipocytes mediate  $\beta$ -selective agonist-induced effects on energy expenditure, insulin secretion, and food intake. A study using transgenic and gene knockout mice. *J. Biol. Chem.* **272**, 17686–17693 (1997).
57. Schneeberger, M. et al. Regulation of energy expenditure by brainstem GABA neurons. *Cell* **178**, 672–685 e612 (2019).
58. Bartness, T. J., Kay Song, C., Shi, H., Bowers, R. R. & Foster, M. T. Brain-adipose tissue cross talk. *Proc. Nutr. Soc.* **64**, 53–64 (2005).
59. Ryu, V., Watts, A. G., Xue, B. & Bartness, T. J. Bidirectional crosstalk between the sensory and sympathetic motor systems innervating brown and white adipose tissue in male Siberian hamsters. *Am. J. Physiol. Regul. Integr. Comp. Physiol.* **312**, R324–R337 (2017).
60. You, H., Chu, P., Guo, W. & Lu, B. A subpopulation of Bdnf-e1-expressing glutamatergic neurons in the lateral hypothalamus critical for thermogenesis control. *Mol. Metab.* **31**, 109–123 (2020).
61. Ryu, V., Garretson, J. T., Liu, Y., Vaughan, C. H. & Bartness, T. J. Brown adipose tissue has sympathetic-sensory feedback circuits. *J. Neurosci.* **35**, 2181–2190 (2015).
62. Farrant, M. & Nusser, Z. Variations on an inhibitory theme: phasic and tonic activation of GABA(A) receptors. *Nat. Rev. Neurosci.* **6**, 215–229 (2005).
63. Bhattarai, J. P. et al. Tonic extrasynaptic GABA(A) receptor currents control gonadotropin-releasing hormone neuron excitability in the mouse. *Endocrinology* **152**, 1551–1561 (2011).
64. Lee, S. et al. Channel-mediated tonic GABA release from glia. *Science* **330**, 790–796 (2010).
65. Park, J. H. et al. Newly developed reversible MAO-B inhibitor circumvents the shortcomings of irreversible inhibitors in Alzheimer's disease. *Sci. Adv.* **5**, eaav0316 (2019).
66. Recena Aydos, L. et al. Nonalcoholic fatty liver disease induced by high-fat diet in C57bl/6 models. *Nutrients* **11**, 3067 (2019).
67. Burdakov, D. & Karnani, M. M. Ultra-sparse connectivity within the lateral hypothalamus. *Curr. Biol.* **30**, 4063–4070 e4062 (2020).
68. Jennings, J. H. et al. Visualizing hypothalamic network dynamics for appetitive and consummatory behaviors. *Cell* **160**, 516–527 (2015).
69. Elias, C. F. et al. Melanin-concentrating hormone projections to areas involved in somatomotor responses. *J. Chem. Neuroanat.* **35**, 188–201 (2008).
70. Harthoorn, L. F., Sane, A., Nethe, M. & Van Heerikhuizen, J. J. Multi-transcriptional profiling of melanin-concentrating hormone and orexin-containing neurons. *Cell. Mol. Neurobiol.* **25**, 1209–1223 (2005).
71. Bamshad, M., Song, C. K. & Bartness, T. J. CNS origins of the sympathetic nervous system outflow to brown adipose tissue. *Am. J. Physiol.* **276**, R1569–R1578 (1999).
72. Bartness, T. J., Vaughan, C. H. & Song, C. K. Sympathetic and sensory innervation of brown adipose tissue. *Int. J. Obes.* **34**, S36–S42 (2010).
73. Richard, D. & Picard, F. Brown fat biology and thermogenesis. *Front. Biosci.* **16**, 1233–1260 (2011).
74. Izawa, S. et al. Melanin-concentrating hormone-producing neurons in the hypothalamus regulate brown adipose tissue and thus contribute to energy expenditure. *J. Physiol.* <https://doi.org/10.1113/jp281241> (2021).
75. Morrison, S. F., Madden, C. J. & Tupone, D. Central neural regulation of brown adipose tissue thermogenesis and energy expenditure. *Cell Metab.* **19**, 741–756 (2014).
76. Nguyen, N. L., Randall, J., Banfield, B. W. & Bartness, T. J. Central sympathetic innervations to visceral and subcutaneous white adipose tissue. *Am. J. Physiol. Regul. Integr. Comp. Physiol.* **306**, R375–R386 (2014).
77. Morrison, S. F., Madden, C. J. & Tupone, D. Central control of brown adipose tissue thermogenesis. *Front. Endocrinol.* **3**, 5 (2012).
78. Pandit, S. et al. Bestrophin1-mediated tonic GABA release from reactive astrocytes prevents the development of seizure-prone network in kainate-injected hippocampi. *Glia* **68**, 1065–1080 (2020).
79. Chun, H., Lim, J., Park, K. D. & Lee, C. J. Inhibition of monoamine oxidase B prevents reactive astrogliosis and scar formation in stab wound injury model. *Glia* <https://doi.org/10.1002/glia.24110> (2021).

80. Nam, M. H. et al. KDS2010, a newly developed reversible MAO-B inhibitor, as an effective therapeutic candidate for Parkinson's disease. *Neurotherapeutics* **18**, 1729–1747 (2021).
81. Shim, H. S., Park, H. J., Woo, J., Lee, C. J. & Shim, I. Role of astrocytic GABAergic system on inflammatory cytokine-induced anxiety-like behavior. *Neuropharmacology* **160**, 107776 (2019).
82. Sa, M. et al. Unaltered tonic inhibition in the arcuate nucleus of diet-induced obese mice. *Exp. Neurobiol.* **31**, 147–157 (2022).
83. Lee, N., Sa, M., Hong, Y. R., Lee, C. J. & Koo, J. Fatty acid increases cAMP-dependent lactate and MAO-B-dependent GABA production in mouse astrocytes by activating a galphas protein-coupled receptor. *Exp. Neurobiol.* **27**, 365–376 (2018).
84. Chao, D. H. M. et al. Hypothalamic astrocytes control systemic glucose metabolism and energy balance. *Cell Metab.* **34**, 1532–1547.e6 (2022).
85. Chun, H. et al. Severe reactive astrocytes precipitate pathological hallmarks of Alzheimer's disease via  $H_2O_2^-$  production. *Nat. Neurosci.* **23**, 1555–1566 (2020).
86. Cheung, B. M., Cheung, T. T. & Samaranyake, N. R. Safety of antiobesity drugs. *Ther. Adv. Drug Saf.* **4**, 171–181 (2013).
87. Kim, G. W., Lin, J. E., Blomain, E. S. & Waldman, S. A. Antiobesity pharmacotherapy: new drugs and emerging targets. *Clin. Pharmacol. Ther.* **95**, 53–66 (2014).
88. Heo, J. Y. et al. Aberrant tonic inhibition of dopaminergic neuronal activity causes motor symptoms in animal models of Parkinson's disease. *Curr. Biol.* **30**, 276–291 e279 (2020).
89. Chun, H. et al. Severe reactive astrocytes precipitate pathological hallmarks of Alzheimer's disease via  $H_2O_2^-$  production. *Nat. Neurosci.* **23**, 1555–U1542 (2020).
90. Park, Y. G. et al. Protection of tissue physicochemical properties using polyfunctional crosslinkers. *Nat. Biotechnol.* <https://doi.org/10.1038/nbt.4281> (2018).
91. Tschop, M. H. et al. A guide to analysis of mouse energy metabolism. *Nat. Methods* **9**, 57–63 (2011).
92. Virtue, S. & Vidal-Puig, A. GTTs and ITTs in mice: simple tests, complex answers. *Nat. Metab.* **3**, 883–886 (2021).
93. Kwak, H. et al. Astrocytes control sensory acuity via tonic inhibition in the thalamus. *Neuron* **108**, 691–706. e610 (2020).
94. Nam, M. H. et al. Excessive astrocytic GABA causes cortical hypometabolism and impedes functional recovery after subcortical stroke. *Cell Rep.* **32**, 107861 (2020).
95. Woo, D. H. et al. TREK-1 and Best1 channels mediate fast and slow glutamate release in astrocytes upon GPCR activation. *Cell* **151**, 25–40 (2012).

## Acknowledgements

We are grateful to all members of the C.J.L. laboratory at the IBS for helpful discussions and comments. We acknowledge T.S.K. at the Research Solution Center of IBS for help with imaging data using the 3D cell culture imaging microscope. S.J. and S.-Y.K. from Seoul National University for help with the measurement of BAT temperature. S.P. from the Korea Advanced Institute of Science and Technology for help with the ANCOVA analysis. This study was supported by

Center for Cognition and Sociality (IBS-R001-D2) to C.J.L. from the IBS, Republic of Korea. W.K. was supported by a Young Scientist Fellowship (IBS-R001-Y1) from the IBS. J.-W.S. was supported by the NRF (2022R1A2C3005613).

## Author contributions

M.S., E.-S.Y., W.K., M.G.P., H.-J.J., Y.R.Y., M.B., J.-H.L., J.L., W.W., J.K., J.-H.K., Y.S., B.K., H.A. and S.E.L. performed the experiments. K.D.P., P.-G.S., J.-W.S. and C.J.L. supervised the analysis. M.S. and C.J.L. designed all the experiments and wrote the manuscript with input from the co-authors.

## Competing interests

K.D.P. and C.J.L. are inventors on a patent for KDS2010 (US11053190) and related to MAO-B inhibition as an anti-obesity therapy (PCT/KR2015/010104). M.S., K.D.P., and C.J.L. are inventors on a patent for reversible MAO-B inhibitors for treating obesity (KR-10-1746060). These patents have been licensed to Neurobiogen, which develops KDS2010 for the treatment of Alzheimer's disease and obesity. Additionally, C.J.L. and K.D.P. also received honoraria for speaking engagements from Neurobiogen. The other authors declare no conflict of interest.

## Additional information

**Extended data** is available for this paper at <https://doi.org/10.1038/s42255-023-00877-w>.

**Supplementary information** The online version contains supplementary material available at <https://doi.org/10.1038/s42255-023-00877-w>.

**Correspondence and requests for materials** should be addressed to C. Justin Lee.

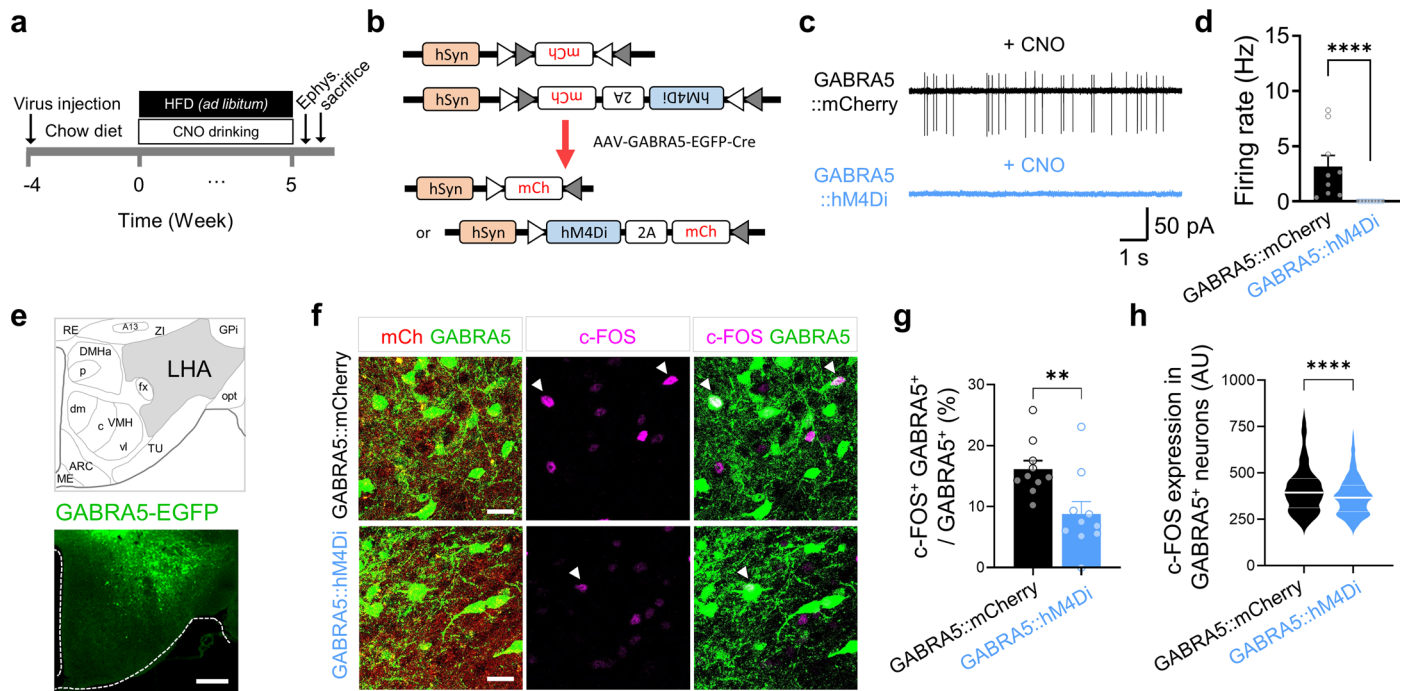
**Peer review information** *Nature Metabolism* thanks Paulo Kofuji for his contribution to the peer review of this work. Primary Handling editor: Ashley Castellanos-Jankiewicz, in collaboration with the *Nature Metabolism* team.

**Reprints and permissions information** is available at [www.nature.com/reprints](http://www.nature.com/reprints).

**Publisher's note** Springer Nature remains neutral with regard to jurisdictional claims in published maps and institutional affiliations.

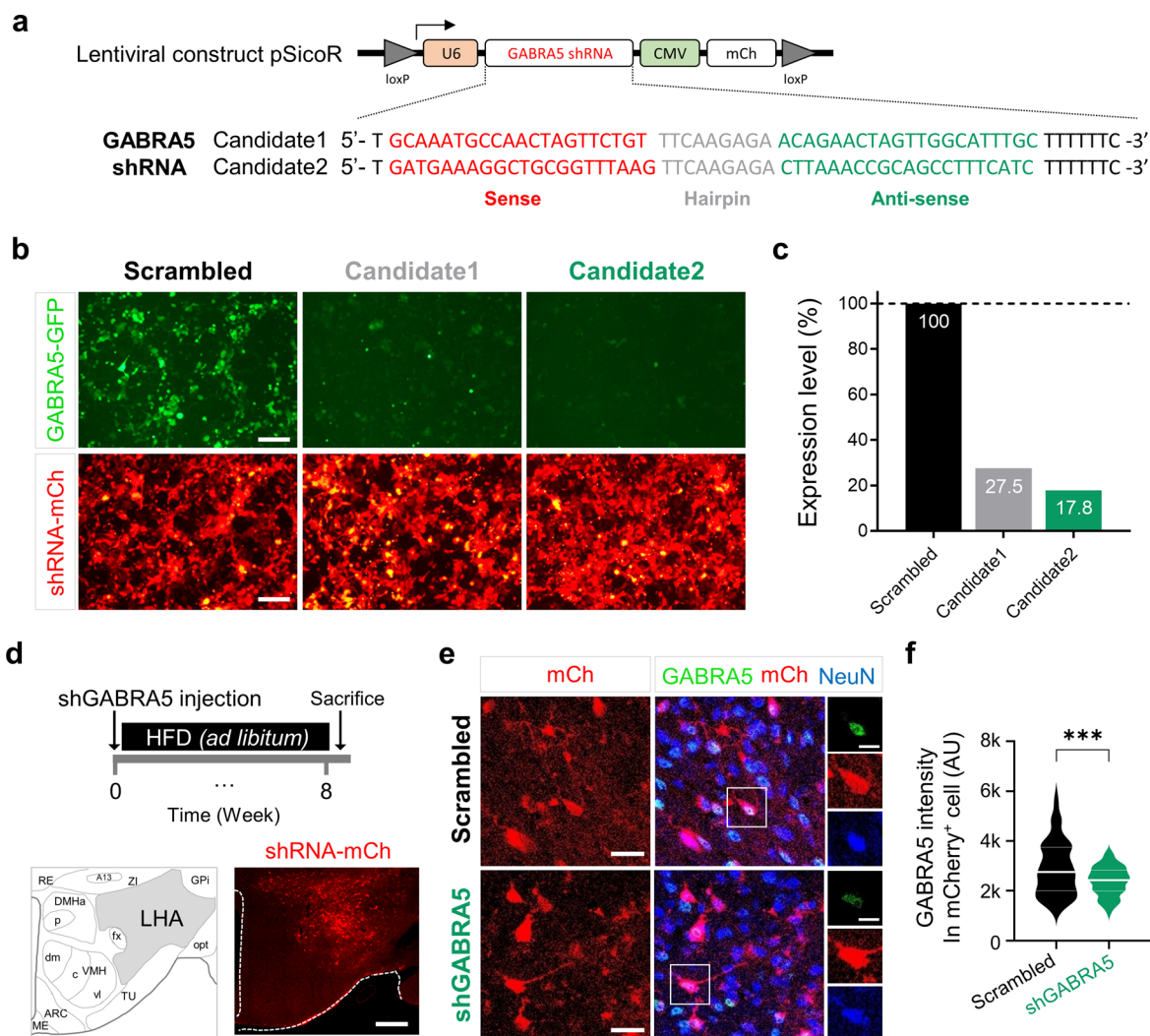
Springer Nature or its licensor (e.g. a society or other partner) holds exclusive rights to this article under a publishing agreement with the author(s) or other rightsholder(s); author self-archiving of the accepted manuscript version of this article is solely governed by the terms of such publishing agreement and applicable law.

© The Author(s), under exclusive licence to Springer Nature Limited 2023, corrected publication 2023



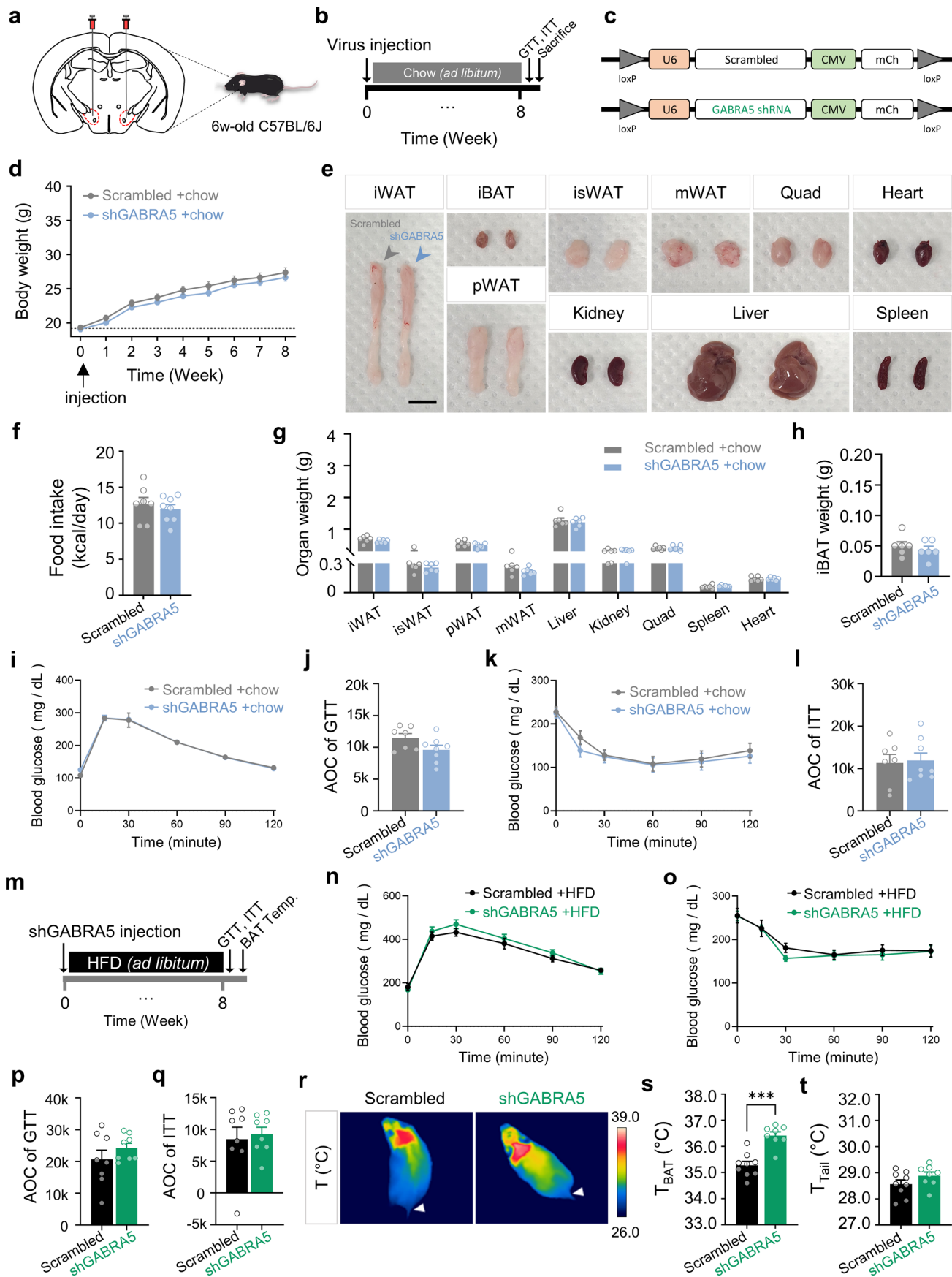
**Extended Data Fig. 1 | Inhibition of GABRA5<sup>LHA</sup> by DREADD.** **a**, Experimental timeline for GABRA5<sup>LHA</sup> under chemogenetic inhibition by DREADD hM4Di with CNO. **b**, GABRA5:mCherry mice were injected with AAV-mGABRA5-EGFP-Cre and Cre-activatable AAV carrying mCh (AAV-hSyn-DIO-mCh). **c**, Ex vivo cell-attached patch-clamp recording of GABRA5<sup>LHA</sup> under chemogenetic inhibition. Representative traces of cell attached recording in GABRA5:mCherry (top) and GABRA5::hM4Di (bottom) in LHA. Both groups were treated of CNO (5  $\mu$ M) with bath application. **d**, Quantification of firing rate in GABRA5:mCherry and GABRA5::hM4Di (n=9, 8 cells, respectively). **e**, Representative images of

AAV-mGABRA5-EGFP-Cre expression in LHA. Scale bar, 100  $\mu$ m. **f**, Representative images of GABRA5:hM4Di and GABRA5:mCherry mice in LHA. Scale bar, 20  $\mu$ m. **g**, Percentage of c-FOS in GABRA5-positive neurons of GABRA5:hM4Di and GABRA5:mCherry mice (n = 10, 10 slices from n = 3, 4 mice, respectively). **h**, Quantification of c-FOS expression in GABRA5-positive neurons in each group (n = 641, 466 cells from n = 3, 4 mice, respectively). Data were presented as mean  $\pm$  SEM. p values were determined by Mann Whitney test (**d,g,h**). \*, p < 0.05; \*\*, p < 0.01; \*\*\*, p < 0.001; \*\*\*\*, p < 0.0001.



**Extended Data Fig. 2 | Development and validation of shRNAs for *Gabra5* *in vitro* and *in vivo*.** **a**, Candidate sequences for GABRA5 shRNA are shown with vector information. Each shRNA was cloned in pSicoR vector to express under U6 promoter together with a cytomegalovirus (CMV) promoter driving expression of mCherry reporter gene. **b**, Fluorescence images of HEK293T cells co-transfected with shRNA vectors (shRNA-mCh, red, bottom) with GABRA5 full clone (GABRA5-GFP, green, top). Scale bar, 100  $\mu$ m. **c**, Gene expression level of *Gabra5* quantified by qRT-PCR in the co-transfected HEK293T cells,

normalized to Scrambled-shRNA. **d**, Schematic and representative images of GABRA5-shRNA-carrying lenti virus express mCherry in LHA. Scale bar, 100  $\mu$ m. **e**, Representative images of GABRA5-IR (GFP) and mCherry in LHA of Scrambled and shGABRA5 group. Scale bar, 20  $\mu$ m. Scale bar, 10  $\mu$ m. **f**, Quantified expression of GABRA5 in mCherry-positive cells in LHA of Scrambled and shGABRA5 group ( $n=96, 64$  cells from  $n=3, 3$  mice, respectively). Data were presented as mean  $\pm$  SEM.  $p$  values were determined by Unpaired t-test (**f**). \*,  $p < 0.05$ ; \*\*,  $p < 0.01$ ; \*\*\*,  $p < 0.001$ ; \*\*\*\*,  $p < 0.0001$ .

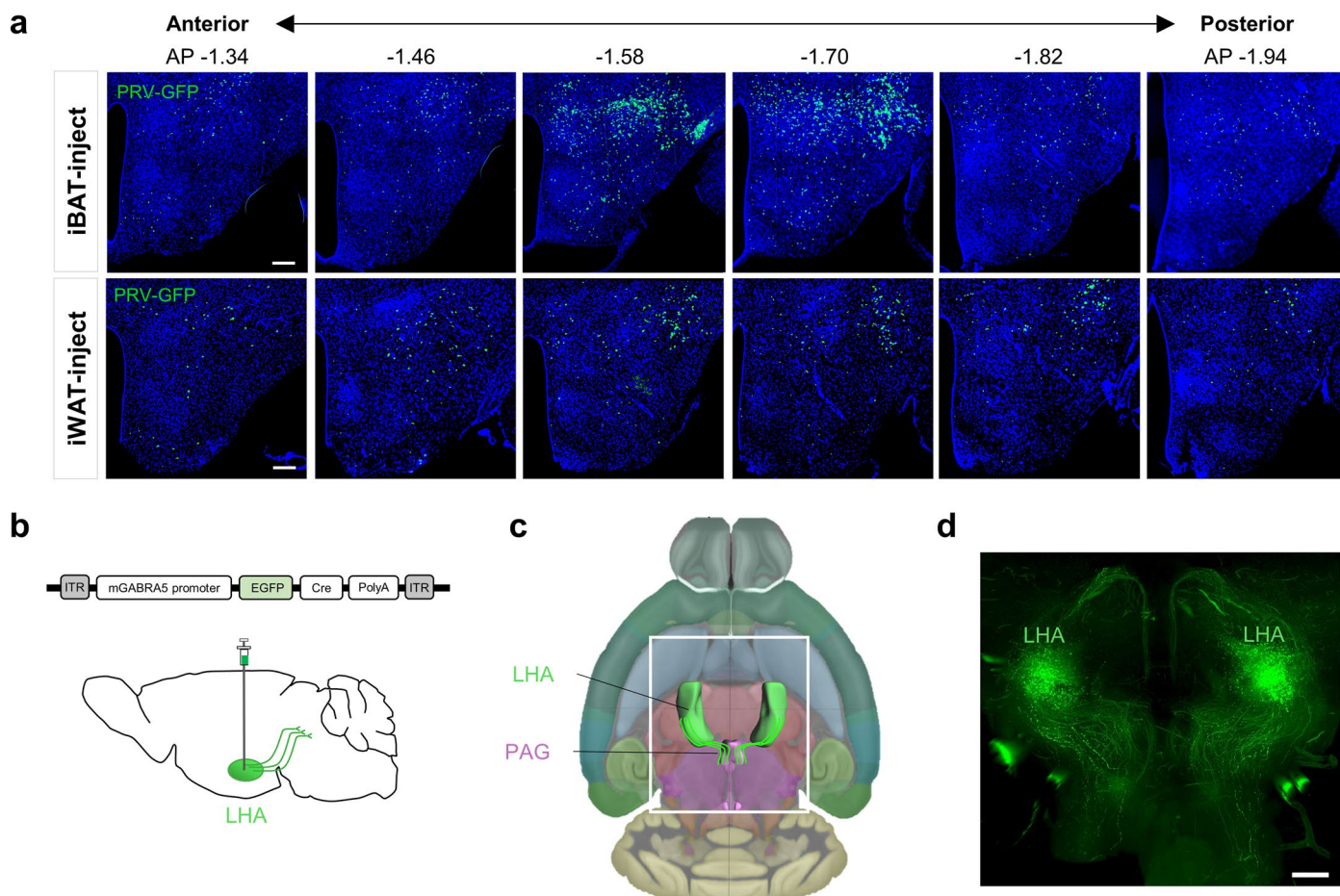


Extended Data Fig. 3 | See next page for caption.

**Extended Data Fig. 3 | Knockdown of Gabra5 in LHA with normal chow diet and HFD. a, b**, Experimental scheme and timeline for LHA injection. **c**, Schematic diagram of Scrambled (top) and shGABRA5 (bottom) virus constructs. **d**, Curves of bodyweight in Scrambled and shGABRA5 mice with chow diet (n = 9, 9 mice per group). **e**, Representative images of each organ between Scrambled and shGABRA5 group with chow diet. Scale bar, 1 cm. **f**, Average food intake per day in Scrambled and shGABRA5 group (n = 7, 8 mice per group). **g**, Quantification of organ weight in Scrambled and shGABRA5 group with chow diet (n = 6 mice per group). **h**, Average weight of iBAT (n = 6 mice per group). **i**, Time course of blood glucose levels during the glucose tolerance test (GTT) in Scrambled and shGABRA5 group with chow diet (n = 7, 8 mice per group). **j**, Quantification of area of curve (AOC) of GTT. **k**, Time course of blood glucose levels during the insulin tolerance test (ITT) in Scrambled and shGABRA5 group with chow diet (n = 7, 8

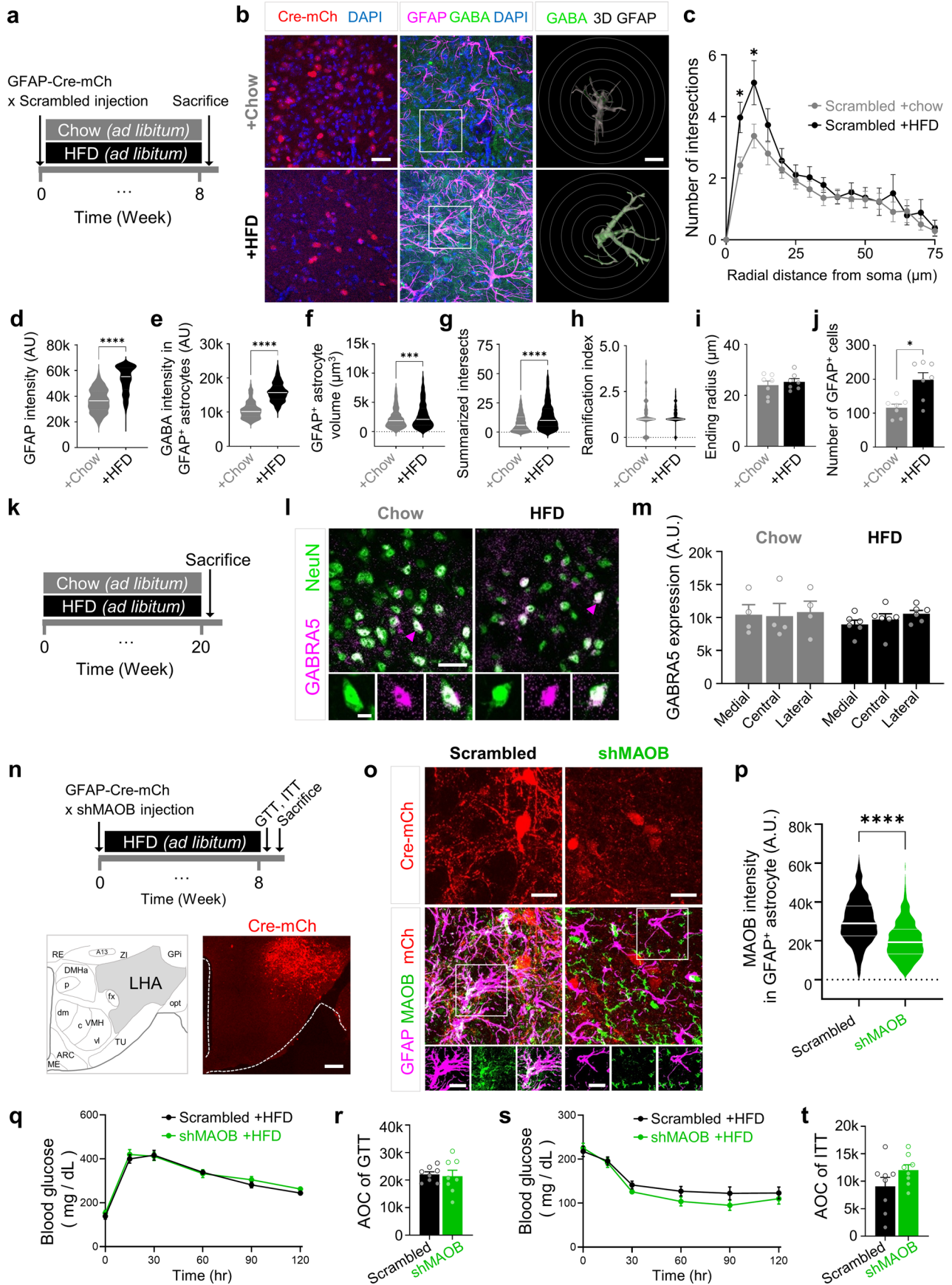
mice per group). **l**, Quantification of area of curve (AOC) of ITT. **m**, Timeline of the experiment. **n**, Time course of blood glucose levels during the glucose tolerance test (GTT) in Scrambled and shGABRA5 group with HFD (n = 8, 8 mice per group). **o**, Time course of blood glucose levels during the insulin tolerance test (ITT) in Scrambled and shGABRA5 group with HFD (n = 8, 8 mice per group). **p**, Quantification of area of curve (AOC) of GTT. **q**, Quantification of area of curve (AOC) of ITT. **r**, Representative infra-red thermograph images showing the surface temperature of the intrascapular brown adipose tissue ( $T_{\text{BAT}}$ ) and the tail temperature ( $T_{\text{Tail}}$ ) in Scrambled and shGABRA5 group (n = 9, 8 mice, respectively). **s**, Quantification of  $T_{\text{BAT}}$ . **t**, Quantification of  $T_{\text{BAT}}$ . Data were presented as mean  $\pm$  SEM. p values were determined by Two-way ANOVA with Šídák's multiple comparisons test (**d, g, i, k, n, o**), Unpaired t-test (**f, p, q, s, t**), or Mann Whitney test (**h, j, l**). \*, p < 0.05; \*\*, p < 0.01; \*\*\*, p < 0.001; \*\*\*\*, p < 0.0001.





**Extended Data Fig. 4 | Expression of iBAT or iWAT innervating neurons in LHA and expression of  $GABRA5^{LHA}$ . Related to Supplementary Movie S1.**  
**a**, Fluorescence images of serial sections along the AP axis of LHA from mice injected with PRV-EGFP virus in iBAT and iWAT 5 days after injection. Sections from AP -1.34 mm to AP -1.94 mm were stained with DAPI (blue). Scale bar,

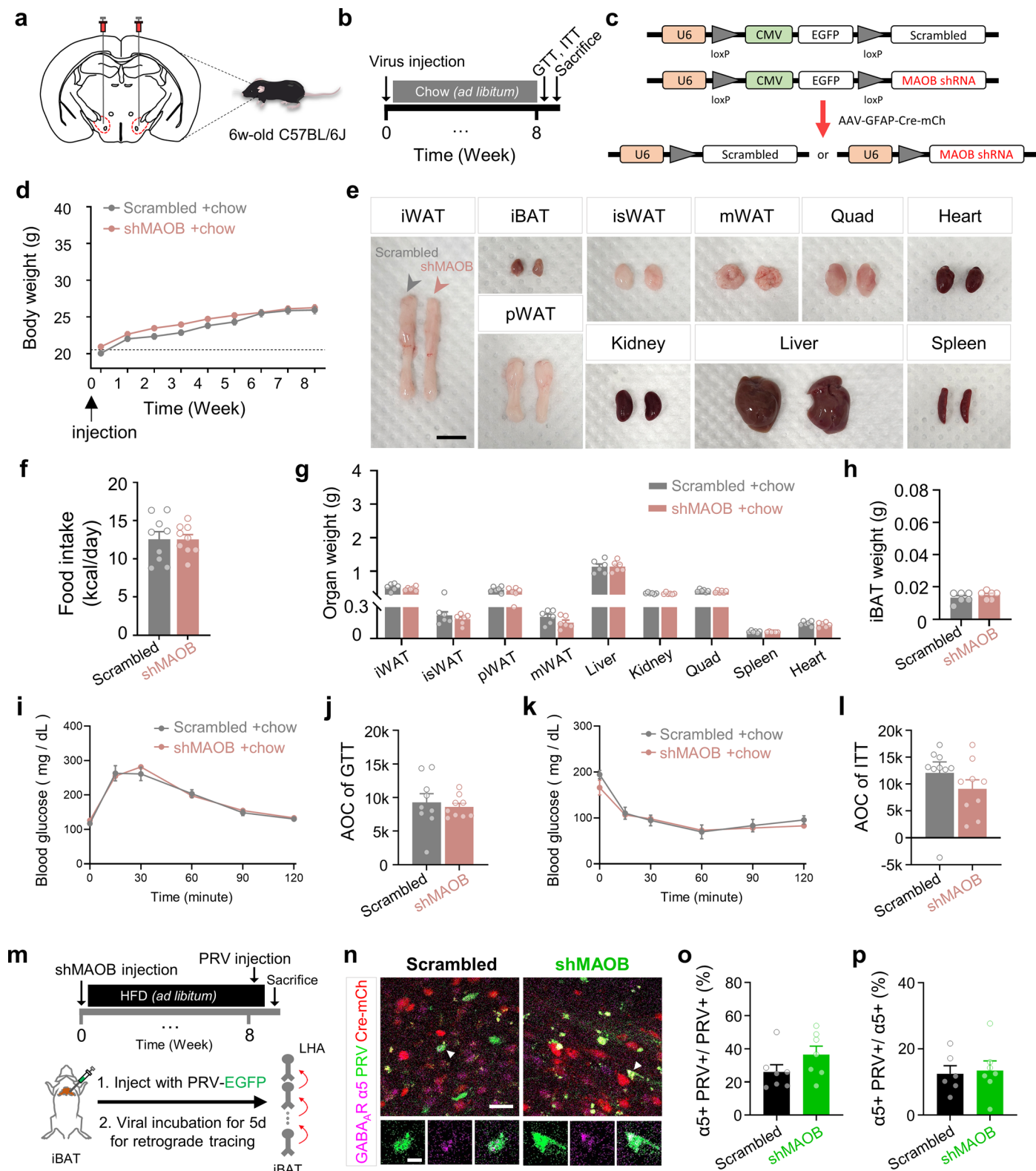
100  $\mu$ m. **b**, Experimental scheme of AAV-mGABRA5-EGFP-Cre virus injection and sagittal view of the mouse brain. **c**, Ventral view of the mouse brain from 3D Allen brain atlas. LHA is colored green and PAG is colored magenta. White rectangle indicates the region of interest. **d**, Ventral image of LHA-injected mice bilaterally with AAV-mGABRA5-EGFP-Cre virus. Scale bar, 300  $\mu$ m.



Extended Data Fig. 5 | See next page for caption.

**Extended Data Fig. 5 | Astrocytes in LHA show hypertrophy in moderate obesity.** **a**, Timeline of the experiment. **b**, Left, Immunostaining for GFAP-Cre-mCh (red) in LHA of Chow and HFD group. Middle, GFAP (magenta), GABA (green), DAPI (blue) in LHA of Chow and HFD group. Scale bar, 30  $\mu\text{m}$ . Right, magnified images taken from the boxed areas in the middle images with 3D rendering, showing GFAP colocalized with GABA immunostaining. Scale bar, 15  $\mu\text{m}$ . **c**, The number of process intersections at each radial distance from soma in GFAP+ astrocytes in each group ( $n = 7$ , 7 slices from 3 chow mice, 3 HFD mice). **d,e**, Quantification of GFAP intensity (**d**) and GABA intensity ( $n = 445$ , 438 cells from 3 chow mice, 3 HFD mice) (**e**) in GFAP+ astrocytes ( $n = 372$ , 438 cells from 3 chow mice, 3 HFD mice). **f**, Quantification for 3D volumes of GFAP+ astrocytes in each group ( $n = 776$ , 1103 cells from 3 chow mice, 3 HFD mice). **g**, Number of summarized intersections of GFAP+ astrocytes in each group ( $n = 734$ , 1299 cells from 3 chow mice, 3 HFD mice). **h**, Quantification of ramification index ( $n = 793$ , 1285 cells from 3 chow mice, 3 HFD mice). **i**, The ending radius of GFAP+ astrocytes in LHA ( $n = 7$ , 7 slices from 3 chow mice, 3 HFD mice). **j**, The number of GFAP+ astrocytes in LHA ( $n = 7$ , 7 slices from 3 chow mice, 3 HFD mice).

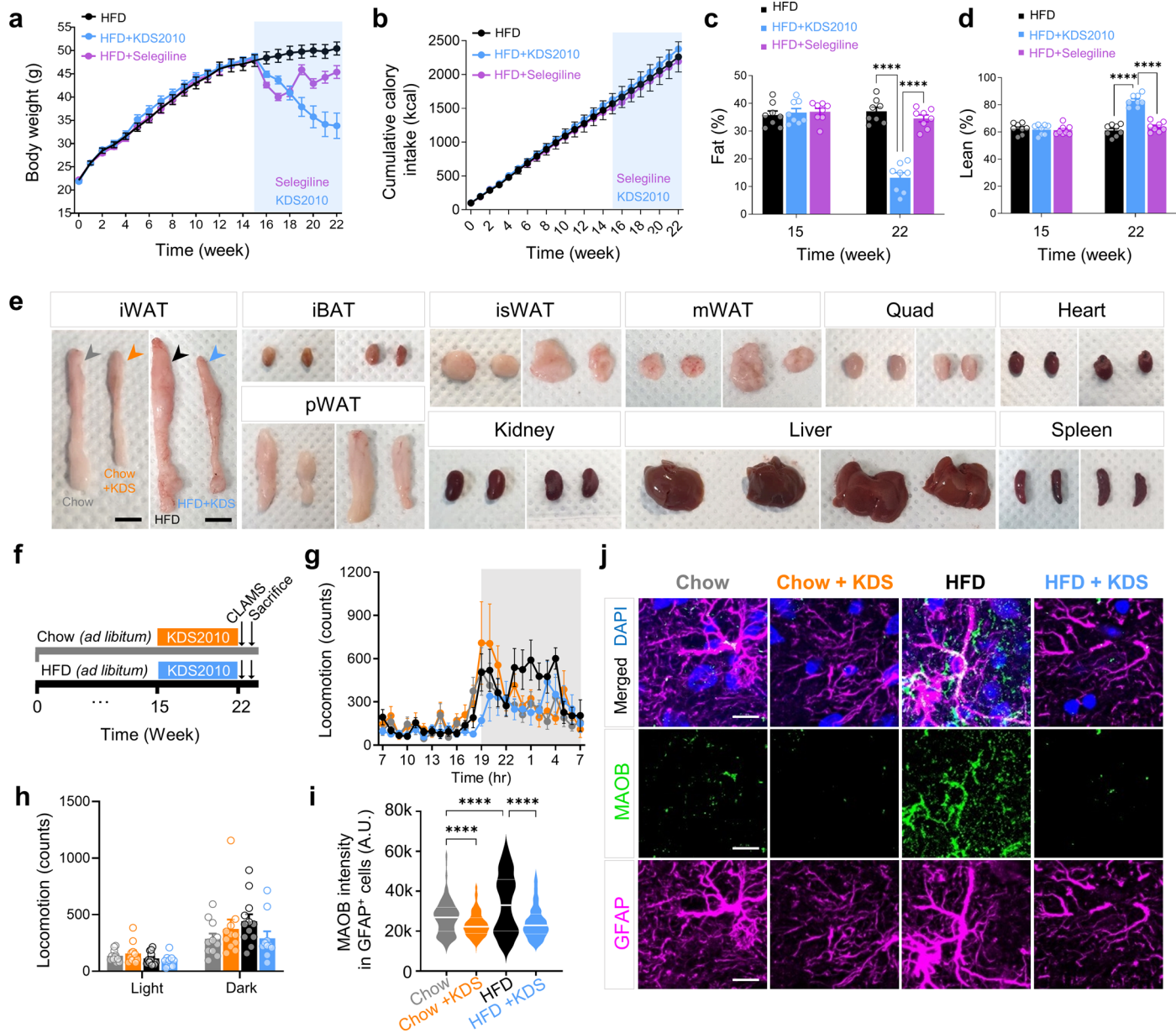
**k**, Timeline of the experiment. **l**, GABRA5 expression in LHA of Chow and HFD mice. **m**, Expression level of GABRA5 in medial, central and lateral part of the LHA was not significantly changed in HFD mice compared to chow mice. Scale bar, 20  $\mu\text{m}$ . Scale bar, 5  $\mu\text{m}$ . **n**, Top, schematic diagram. Bottom, GABRA5-shRNA-carrying lenti virus express mCherry in LHA. Scale bar, 100  $\mu\text{m}$ . **o**, Maob-IR was shown in GFP. Scale bar, 20  $\mu\text{m}$ . Scale bar, 15  $\mu\text{m}$ . **p**, Expression of Maob in GFAP-positive astrocytes in LHA was significantly lower in shMAOB group compared to Scrambled group ( $n = 697$ , 345 cells from 3, 3 mice, respectively). **q**, Time course of blood glucose levels during the glucose tolerance test (GTT) in Scrambled and shMAOB group with HFD ( $n = 8$ , 8 mice, respectively). **r**, Quantification of area of curve (AOC) of GTT. **s**, Time course of blood glucose levels during the insulin tolerance test (ITT) in Scrambled and shMAOB group with HFD ( $n = 8$ , 8 mice per group). **t**, Quantification of area of curve (AOC) of ITT. Data were presented as mean  $\pm$  SEM. p values were determined by Two-way ANOVA with Šidák's multiple comparisons test (**c,q,s**), Mann-Whitney test (**d-j,p**), or Unpaired t-test (**r,t**). \*,  $p < 0.05$ ; \*\*,  $p < 0.01$ ; \*\*\*,  $p < 0.001$ ; \*\*\*\*,  $p < 0.0001$ .



Extended Data Fig. 6 | See next page for caption.

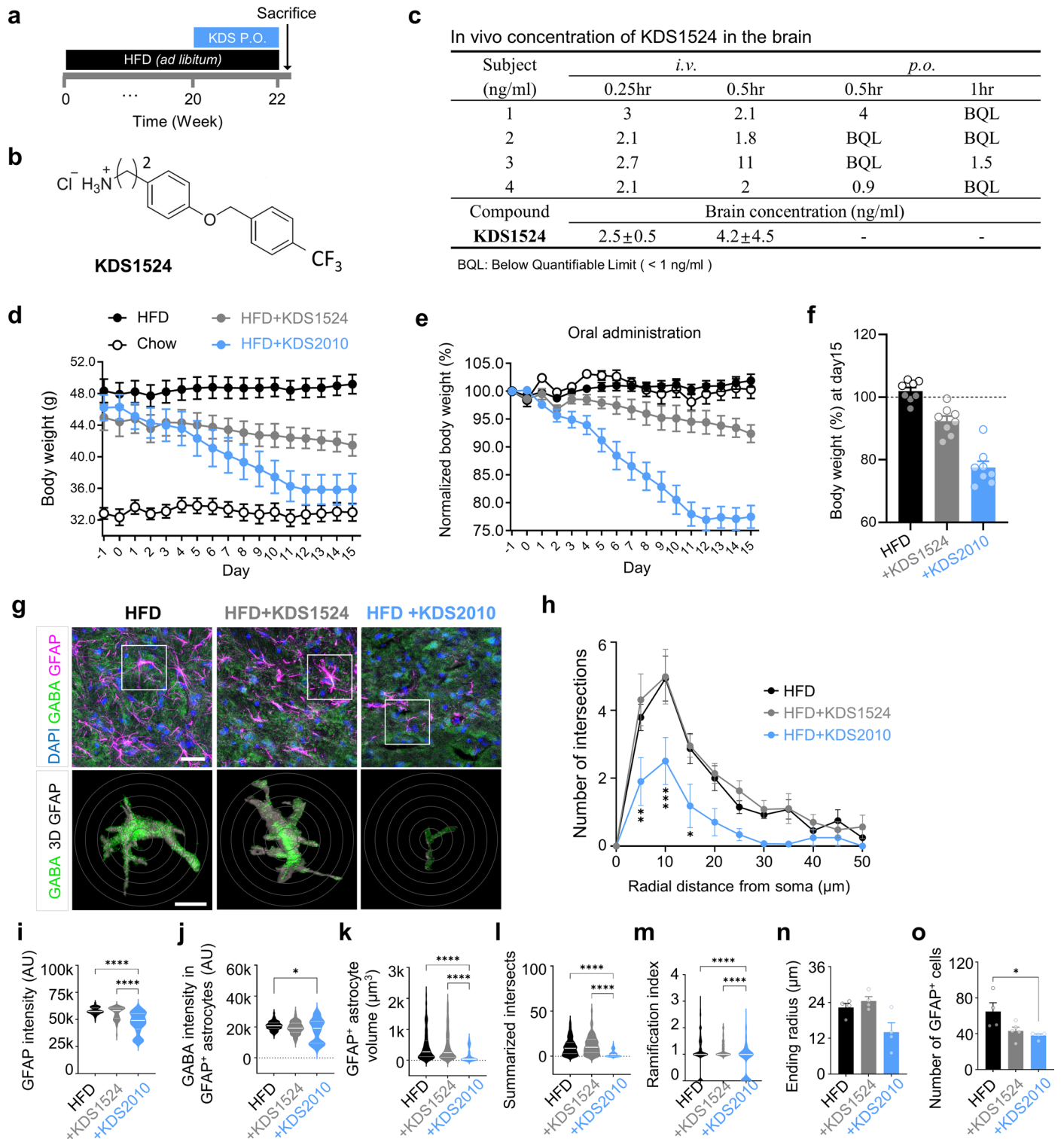
**Extended Data Fig. 6 | Knockdown of astrocytic Maob in LHA with normal chow diet and HFD. a,b**, Experimental scheme and timeline for LHA injection. **c**, Schematic diagram of Scrambled (top) and shMAOB (bottom) virus constructs. **d**, Curves of bodyweight in Scrambled and shMAOB group with chow diet (n = 9, 10 mice per group). **e**, Representative images of each organ between Scrambled and shMAOB group with chow diet. Scale bar, 1 cm. **f**, Average food intake per day in Scrambled and shMAOB group (n = 9, 10 mice per group). **g**, Quantification of organ weight in Scrambled and shMAOB group with chow diet (n = 6, 6 mice per group). **h**, Average weight of iBAT (n = 6, 6 mice per group). **i**, Time course of blood glucose levels during the glucose tolerance test (GTT) in Scrambled and shMAOB group with chow diet (n = 9, 9 mice per group). **j**, Quantification of area

of curve (AOC) of GTT. **k**, Time course of blood glucose levels during the insulin tolerance test (ITT) in Scrambled and shMAOB group with chow diet (n = 9, 9 mice per group). **l**, Quantification of area of curve (AOC) of ITT. **m**, Timeline and schematic images of the experiment. **n**, Representative images of LHA from PRV-EGFP injected (green) mice stained against GABA<sub>A</sub>R- $\alpha$ 5 (magenta) with Cre signals (top). Scale bar, 50  $\mu$ m. Magnification of arrowed cells (bottom). Scale bar, 10  $\mu$ m. **o,p**, Quantification between GABRA5 and PRV retrogradely labeled from iBAT at 5 days post-injection (n = 6, 7 slices from 3, 3 mice per group). Data were presented as mean  $\pm$  SEM. p values were determined by Two-way ANOVA with Šidák's multiple comparisons test (**d,g,i,k**), Unpaired t-test (**f,j,l**), or Mann-Whitney test (**h,l,o,p**). \*, p < 0.05; \*\*, p < 0.01; \*\*\*, p < 0.001; \*\*\*\*, p < 0.0001.



**Extended Data Fig. 7 | KDS2010 reduces astrocytic Maob and fats without affecting locomotion.** **a**, Curves representing the kinetics of change in body weight among HFD, HFD with KDS2010, and HFD with selegiline mice over the 22 weeks following HFD treatment. Light blue shaded box indicates period of KDS2010 or selegiline treatment in drinking water (n=8, 8, 8, and 8 mice, respectively). **b**, Cumulative food intake in HFD, HFD with KDS2010, HFD with selegiline mice over the 22 weeks (n=8, 8, 8, and 8 mice, respectively). **c,d**, Quantification of percentage change of fat mass (**c**) and lean mass (**d**) before (at 15 weeks) and after (at 22 weeks) KDS2010 or selegiline treatment (n=8, 8, 8, and 8 mice, respectively). **e**, Representative images of each organ of chow, chow with KDS2010, HFD, HFD with KDS2010 mice. Scale bar, 1 cm. **f**, Timeline of the

experiment. **g**, Real-time monitoring curve of locomotion in chow, KDS2010-treated chow, HFD, and KDS2010-treated HFD mice (n=11, 11, 12, and 10 mice for respective group). **h**, Quantification of locomotor activity in light and dark cycle. **i**, Quantification of Maob intensity in GFAP-positive cells in chow, chow with KDS2010, HFD, and HFD with KDS2010 group (n=464, 463, 337, and 296 cells from 4, 4, 3, and 3 mice per group, respectively). **j**, Representative images for Maob (green) and GFAP (magenta) in LHA of chow, chow with KDS2010, HFD, and HFD with KDS2010 group. Scale bar, 10  $\mu$ m. Data were presented as mean  $\pm$  SEM. p values were determined by One-way ANOVA with Tukey's multiple comparisons test (**c,d,h**) or Kruskal-Wallis test (**i**). \*, p < 0.05; \*\*, p < 0.01; \*\*\*, p < 0.001; \*\*\*\*, p < 0.0001.

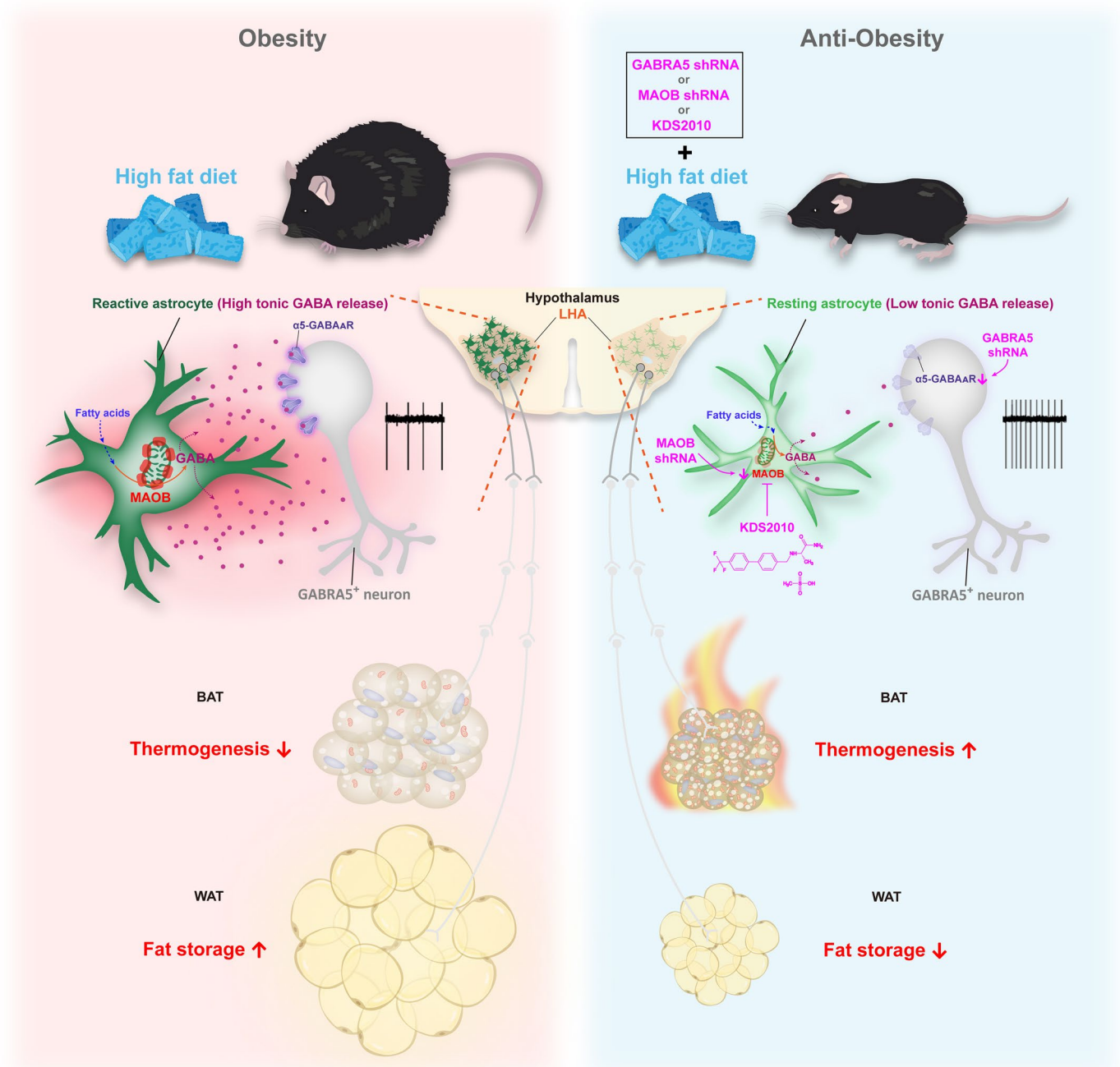


Extended Data Fig. 8 | See next page for caption.

**Extended Data Fig. 8 | A less-BBB-permeable Maob inhibitor, KDS1524 does not reduce astrogliosis in LHA.** **a**, Experimental timeline for oral administration of KDS2010 or KDS1524 with HFD. **b**, Chemical structure of KDS1524. **c**, Cerebrospinal fluid (CSF) concentration after intravenous and oral administration at a dose of 5, 10 mg/kg of KDS1524 (n = 4 rat). **d**, Curves representing the kinetics of change in body weight in gram of chow, HFD, HFD with KDS1524 and HFD with KDS2010 mice over 16 days following HFD treatment. KDS2010 or KDS1524 was administered by oral injection (n = 8, 8, 8, and 8 mice, respectively). **e**, Curves representing the kinetics of change in body increase in the percentage of chow, HFD, HFD with KDS1524 and HFD with KDS2010 mice (n = 8, 8, 8, and 8 mice, respectively). **f**, Quantification of percentage change of body increase of HFD with KDS1524 and HFD with KDS2010 compared to HFD mice. **g**, Top, Immunostaining for GABA (green) and GFAP (magenta) in LHA of HFD, HFD with KDS1524 and HFD with KDS2010 group. Scale bar, 30  $\mu$ m. Bottom, magnified images taken from the boxed areas in the top images with 3D

rendering, showing GFAP colocalized with GABA immunostaining. Scale bar, 15  $\mu$ m. **h**, The number of process intersections at each radial distance from soma in GFAP<sup>+</sup> astrocytes in each group (n = 4, 5, and 4 slices from 4, 4, and 4 mice). **i, j**, Quantification of GFAP intensity (n = 88, 116, and 68 cells) (**i**) and GABA intensity (n = 118, 93, and 65 cells) (**j**) in GFAP<sup>+</sup> astrocytes from 4, 4, and 4 mice, respectively. **k, l**, Quantification for 3D volumes (n = 323, 318, and 104 cells) (**k**), number of summarized intersections (n = 234, 160, and 165 cells) (**l**) of GFAP<sup>+</sup> astrocytes from 4, 4, and 4 mice, respectively. **m**, Quantification of ramification index (n = 235, 180, and 190 cells from 4, 4, and 4 mice, respectively). **n**, The ending radius of GFAP<sup>+</sup> astrocytes in LHA (n = 4, 4, and 4 slices per group from 4, 4, and 4 mice). **o**, The number of GFAP<sup>+</sup> astrocytes in LHA (n = 4, 5, and 4 slices per group from 4, 4, and 4 mice). Data were presented as mean  $\pm$  SEM. p values were determined by Two-way ANOVA with Tukey's multiple comparisons test (**h**) or One-way ANOVA with Kruskal-Wallis test (**i, j, k, l, m, n, o**). \*, p < 0.05; \*\*, p < 0.01; \*\*\*, p < 0.001; \*\*\*\*, p < 0.0001.





**Extended Data Fig. 9 | Model of obesity and anti-obesity mechanisms.** Left, in the chronic HFD-fed DIO mouse model, the expression of the GABA-synthesizing enzyme, *Maob*, increases in reactive astrocytes within the LHA. This elevated astrocytic GABA production leads to the tonic suppression of GABAergic GABRA5<sup>LHA</sup> activity. The subsequent inhibition of pacemaker firing in GABRA5<sup>LHA</sup> exacerbates obesity by reducing thermogenesis and lipolysis in both BAT and

WAT. Right, the elevated tonic inhibition can be reversed by either gene-silencing of *Maob* or pharmacological treatment targeting *Maob*, or by gene-silencing of *Gabra5* in the LHA of the DIO mouse model. These interventions release the inhibition on the pacemaker firing of GABRA5<sup>LHA</sup>, thereby enhancing fat-burning and potentially preventing obesity.

## Reporting Summary

Nature Portfolio wishes to improve the reproducibility of the work that we publish. This form provides structure for consistency and transparency in reporting. For further information on Nature Portfolio policies, see our [Editorial Policies](#) and the [Editorial Policy Checklist](#).

### Statistics

For all statistical analyses, confirm that the following items are present in the figure legend, table legend, main text, or Methods section.

n/a | Confirmed

- The exact sample size ( $n$ ) for each experimental group/condition, given as a discrete number and unit of measurement
- A statement on whether measurements were taken from distinct samples or whether the same sample was measured repeatedly
- The statistical test(s) used AND whether they are one- or two-sided  
*Only common tests should be described solely by name; describe more complex techniques in the Methods section.*
- A description of all covariates tested
- A description of any assumptions or corrections, such as tests of normality and adjustment for multiple comparisons
- A full description of the statistical parameters including central tendency (e.g. means) or other basic estimates (e.g. regression coefficient) AND variation (e.g. standard deviation) or associated estimates of uncertainty (e.g. confidence intervals)
- For null hypothesis testing, the test statistic (e.g.  $F$ ,  $t$ ,  $r$ ) with confidence intervals, effect sizes, degrees of freedom and  $P$  value noted  
*Give  $P$  values as exact values whenever suitable.*
- For Bayesian analysis, information on the choice of priors and Markov chain Monte Carlo settings
- For hierarchical and complex designs, identification of the appropriate level for tests and full reporting of outcomes
- Estimates of effect sizes (e.g. Cohen's  $d$ , Pearson's  $r$ ), indicating how they were calculated

*Our web collection on [statistics for biologists](#) contains articles on many of the points above.*

### Software and code

Policy information about [availability of computer code](#)

Data collection	We used Imaging WorkBench (version 6.2, version 9.0.4.0.), pClamp (version 10.2, version 10.4), MiniAnalysis (synaptosoft), and Clamfit (Molecular Devices) to collect the electrophysiological data. We used ZEN Digital Imaging for Light Microscopy blue system (version 3.2, Zeiss) to collect the images from immunohistochemistry. For CLAMS analysis, Oxymax for Window software was used.
Data analysis	We used MedCalc (version 20.218) for ANCOVA analysis, ImageJ (version 1.52s, version 1.53c) and IMARIS (version 9.0.1, Oxford Instruments) for images analysis, GraphPad Prism (version 9).

For manuscripts utilizing custom algorithms or software that are central to the research but not yet described in published literature, software must be made available to editors and reviewers. We strongly encourage code deposition in a community repository (e.g. GitHub). See the Nature Portfolio [guidelines for submitting code & software](#) for further information.

## Data

Policy information about [availability of data](#)

All manuscripts must include a [data availability statement](#). This statement should provide the following information, where applicable:

- Accession codes, unique identifiers, or web links for publicly available datasets
- A description of any restrictions on data availability
- For clinical datasets or third party data, please ensure that the statement adheres to our [policy](#)

We deposited the raw data and the statistics in a public repository, Mendeley (<http://data.mendeley.com/>). The data that support the findings of this study are available from the corresponding author upon reasonable request.

## Research involving human participants, their data, or biological material

Policy information about studies with [human participants or human data](#). See also policy information about [sex, gender \(identity/presentation\), and sexual orientation](#) and [race, ethnicity and racism](#).

### Reporting on sex and gender

*Use the terms sex (biological attribute) and gender (shaped by social and cultural circumstances) carefully in order to avoid confusing both terms. Indicate if findings apply to only one sex or gender; describe whether sex and gender were considered in study design; whether sex and/or gender was determined based on self-reporting or assigned and methods used. Provide in the source data disaggregated sex and gender data, where this information has been collected, and if consent has been obtained for sharing of individual-level data; provide overall numbers in this Reporting Summary. Please state if this information has not been collected. Report sex- and gender-based analyses where performed, justify reasons for lack of sex- and gender-based analysis.*

### Reporting on race, ethnicity, or other socially relevant groupings

*Please specify the socially constructed or socially relevant categorization variable(s) used in your manuscript and explain why they were used. Please note that such variables should not be used as proxies for other socially constructed/relevant variables (for example, race or ethnicity should not be used as a proxy for socioeconomic status). Provide clear definitions of the relevant terms used, how they were provided (by the participants/respondents, the researchers, or third parties), and the method(s) used to classify people into the different categories (e.g. self-report, census or administrative data, social media data, etc.) Please provide details about how you controlled for confounding variables in your analyses.*

### Population characteristics

*Describe the covariate-relevant population characteristics of the human research participants (e.g. age, genotypic information, past and current diagnosis and treatment categories). If you filled out the behavioural & social sciences study design questions and have nothing to add here, write "See above."*

### Recruitment

*Describe how participants were recruited. Outline any potential self-selection bias or other biases that may be present and how these are likely to impact results.*

### Ethics oversight

*Identify the organization(s) that approved the study protocol.*

Note that full information on the approval of the study protocol must also be provided in the manuscript.

## Field-specific reporting

Please select the one below that is the best fit for your research. If you are not sure, read the appropriate sections before making your selection.

- Life sciences       Behavioural & social sciences       Ecological, evolutionary & environmental sciences

For a reference copy of the document with all sections, see [nature.com/documents/nr-reporting-summary-flat.pdf](https://nature.com/documents/nr-reporting-summary-flat.pdf)

## Life sciences study design

All studies must disclose on these points even when the disclosure is negative.

Sample size      No statistical method was used to predetermine sample size. Sample size were determined based on prior studies and literature in the field.

Data exclusions      To ensure data integrity and minimize the influence of outliers, an outlier test was performed using a significance threshold of  $Q = 1\%$ . Outliers exceeding this threshold were excluded from the analysis to mitigate their potential influence on the results, ensuring the robustness and reliability of the findings. Additionally, data were excluded on technical basis in specific instances. For example, in Figure 3D, one mouse from each group was excluded due to mis-location of virus expression in a non-targeted area. This exclusion was based on objective criteria and aimed to maintain the accuracy and validity of the experimental outcomes.

Replication      The key findings of the paper were confirmed by multiple complementary experiments. All experiments were conducted with sufficient number of animals that exhibited consistent effects.

Randomization      Mice were randomly assigned to the experimental groups and treated in the same way.

## Reporting for specific materials, systems and methods

We require information from authors about some types of materials, experimental systems and methods used in many studies. Here, indicate whether each material, system or method listed is relevant to your study. If you are not sure if a list item applies to your research, read the appropriate section before selecting a response.

### Materials & experimental systems

n/a	Involvement in the study
<input type="checkbox"/>	<input checked="" type="checkbox"/> Antibodies
<input type="checkbox"/>	<input checked="" type="checkbox"/> Eukaryotic cell lines
<input checked="" type="checkbox"/>	<input type="checkbox"/> Palaeontology and archaeology
<input type="checkbox"/>	<input checked="" type="checkbox"/> Animals and other organisms
<input checked="" type="checkbox"/>	<input type="checkbox"/> Clinical data
<input checked="" type="checkbox"/>	<input type="checkbox"/> Dual use research of concern
<input checked="" type="checkbox"/>	<input type="checkbox"/> Plants

### Methods

n/a	Involvement in the study
<input checked="" type="checkbox"/>	<input type="checkbox"/> ChIP-seq
<input checked="" type="checkbox"/>	<input type="checkbox"/> Flow cytometry
<input checked="" type="checkbox"/>	<input type="checkbox"/> MRI-based neuroimaging

## Antibodies

### Antibodies used

Primary antibodies were added to blocking solution at desired dilution and slices were incubated in a shaker at 4°C overnight. Primary antibodies for immunostaining were rabbit anti-GABRA5 (abcam, ab10098, 1:200), mouse anti-Orexin A (santa cruz biotechnology, sc-80263, 1:100), rabbit anti-Orexin B (abcam, ab255293, 1:500), rabbit anti-MCH (H-070-47, 1:200), guinea pig anti-GABA (millipore, AB175, 1:200), chicken anti-GFAP (millipore, AB5541, 1:500), rabbit-S100 $\beta$  (abcam, ab52642, 1:200), mouse anti-Maob (santa cruz biotechnology, sc-515354, 1:100), guinea pig anti-NeuN (millipore, ABN90, 1:500), mouse anti-NeuN (millipore, MAB377) and rabbit anti-c-fos (cell signaling, 2250S, 1:500). Secondary antibodies for immunostaining were donkey anti-rabbit Alexa Fluor 488 (Jackson, 711-547-003, 1:200), donkey anti-chicken IgG Alexa Fluor 405 (Jackson, 703-475-155, 1:200), donkey anti-rabbit Alexa Fluor 594 (Jackson, 711-585-152, 1:200), donkey anti-rabbit Alexa Fluor 647 (Jackson, 711-605-152, 1:200), donkey anti-guinea pig Alexa Fluor 647 (Jackson, 706-605-148, 1:200).

### Validation

All antibodies used in this study were bought from formal biological company with applied and described in previously scientific publications. Rabbit anti-Gabra5 antibody (<https://www.citeab.com/antibodies/731866-ab10098-anti-gaba-a-receptor-alpha-5-gabra5-antibody>), mouse anti-Orexin A antibody (Wang et al., Cell, 2021), rabbit anti-Orexin B antibody (<https://www.abcam.com/orexin-b-antibody-epr22803-18-ab255293.html>), rabbit anti-MCH antibody (Obukuro et al., J Neurosci., 2013), guinea pig anti-GABA antibody (Chun et al., Glia, 2021), chicken anti-GFAP antibody (Chun et al., Glia, 2021), rabbit anti-S100 $\beta$  antibody (<http://www.abcam.com/s100-beta-antibody-ab41548.html>), mouse anti-Maob antibody (Fecher et al., nat. neurosci. 2019), mouse anti-NeuN antibody (<https://www.citeab.com/antibodies/226230-mab377-anti-neun-antibody-clone-a60>), guinea pig anti-NeuN antibody (<https://www.citeab.com/antibodies/226230-mab377-anti-neun-antibody-clone-a60>), rabbit anti-c-fos antibody (<https://www.biocompare.com/9776-Antibodies/1540778-cFos-9F6-Rabbit-mAb/>).

## Eukaryotic cell lines

Policy information about [cell lines and Sex and Gender in Research](#)

### Cell line source(s)

HEK293T cells were purchased from ATCC (CRL-3216).

### Authentication

HEK293T cell line was not authenticated in our hands for this manuscript but was obtained and used from <https://www.atcc.org/products/crl-3216>.

### Mycoplasma contamination

All cell lines tested negative for mycoplasma contamination.

### Commonly misidentified lines (See [ICLAC](#) register)

No commonly misidentified cell lines were used.

## Animals and other research organisms

Policy information about [studies involving animals; ARRIVE guidelines](#) recommended for reporting animal research, and [Sex and Gender in Research](#)

### Laboratory animals

All experiments performed on diet-induced obesity (DIO) mouse model were performed on C57BL/6J background. The mice were used originated from Jackson Laboratory (USA, stock number 000664). 6-week-old male C57BL/6J mice (DBL, Chungbuk, Republic of Korea) were fed a HFD (60% kcal fat, D12492, Research Diets Inc.) or chow (Teklad, 2018S, Envigo) for 6~23 weeks. All mice were maintained in a specific pathogen-free under controlled animal facility. These conditions included a 12-h light-dark cycle with lights on at 8:00 AM at a temperature of 21°C, and a humidity range of 40% to 60%. The mice were allowed free access to water and food.

Wild animals

This study does not involve wild animals.

Reporting on sex

The findings apply to male mice only.

Field-collected samples

This study does not involve field-collected sample.

Ethics oversight

All animal experiments were performed according to procedures approved by the Institutional Animal Care and Use Committee of IBS (Daejeon, South Korea) and Korea Institute of Science and Technology (Seoul, South Korea).

Note that full information on the approval of the study protocol must also be provided in the manuscript.